

A Search for Exoplanet Candidates in TESS short cadence Lightcurves with Bayesian Detection

JAMILA S. TAAKI,¹ ATHOL J. KEMBALL,² AND FARZAD KAMALABADI¹

¹*Department of Electrical and Computer Engineering, University of Illinois at Urbana-Champaign
306 N. Wright St. MC 702, Urbana, IL 61801-2918*

²*Department of Astronomy, University of Illinois at Urbana-Champaign
1002 W. Green Street, Urbana, IL 61801-3074*

Submitted to ApJ

ABSTRACT

Lightcurves produced by transit surveys are significantly impacted by systematic noise, which without further processing, conceals exoplanet transit signals. Methods for transit detection in the presence of both systematic and stellar noise are derived in Taaki et al. (2020). The detectors use Bayesian priors to model unknown systematic noise and stellar variability incorporated in a Neyman-Pearson optimal likelihood ratio test for a candidate transit signal. Herein we apply this detection method to search for exoplanet transit signals with periods between 1 and 100 days in 3 years of TESS 2 min cadence lightcurve data from all targets persistent within the continuous viewing zone. We produce a detection pipeline which addresses several data- challenges for TESS data. Pre-processing and computation methods are designed for increased data density and data gaps. Post-processing statistics are introduced to filter false alarms occurring due to TESS systematic noise properties. The theoretical detection performance for TESS data is evaluated with simulated injection tests, where the joint Bayesian detector achieves a 79 % detection efficiency at $\tau = 10$ threshold. A total of 5535 targets continuously observed over at least a year of data were searched for exoplanet transits, with detections occurring in approximately 28% of lightcurves. Among these we recover 77% of TESS-Objects-of-Interest present with matching orbital period. Furthermore we present a vetted list of 16 new candidate exoplanets.

Keywords: exoplanets — exoplanet detection methods — transit photometry — Bayesian statistics

1. INTRODUCTION

The Transiting Exoplanet Survey Satellite (TESS)¹ (Ricker et al. 2014) was launched in 2018 to survey $\sim 10^6$ nearby stars for planets. TESS is the successor to two-decades of wide-field surveys: primarily CoRoT² (Auvergne et al. 2009) and Kepler³ (Borucki et al. 2010). Statistical inference and data-processing algorithms have been key in achieving the necessary precision to detect a wide-range of exoplanet signals and process the vast quantity of data collected by transit surveys (Jara-Maldonado et al. 2020). In particular, a number of specialized approaches have been developed to mitigate the effect of instrumental noise which may otherwise mask astrophysical signals in lightcurves (Twicken et al. 2010; Smith et al. 2012; Stumpe et al. 2012, 2014; Roberts et al. 2013; Aigrain et al. 2016; Foreman-Mackey et al. 2015). In this work we modify and apply a detection method for lightcurve containing systematic and stochastic noise due to Taaki et al. (2020) to search TESS 2-minute lightcurves for candidate exoplanets.

Each year TESS focuses on the North or South ecliptic poles, returning every other year to the same pole. Observations are broken into approximate 27-day sectors, over which data is collected for a fixed $24'' \times 96''$ field. The

Corresponding author: Jamila Taaki
xiazinya@gmail.com

¹ tess.mit.edu

² sci.esa.int/corot

³ keplerscience.arc.nasa.gov

telescope rotates to observe a new field over the next sector. A small subset of targets are continuously observed for the full year (13 sectors) in a region termed the Continuous Viewing Zone (CVZ). Every 30-minutes full-frame images are produced, which are analysed by the Quick-Look-Pipeline (QLP) (Huang et al. 2020). The Science Processing Operations Center (SPOC) pipeline Twicken et al. (2019) produces 2 min cadence lightcurve data for a list of targets (provided by the TESS Input Catalog (TIC) ⁴), selected for the potential for sub-Neptune discoveries (Stassun et al. 2018). In each sector approximately 16000+ lightcurves are produced, with 200,000 stellar targets observed in a year and ~ 2000 continuously observed for a full year. To date there have been 5210 TESS Objects of Interest (TOI) released, 1191 of which due to the SPOC pipeline, a total of 180 TOI are confirmed exoplanets⁵.

In this work we apply our Bayesian detection method to TESS data, focused on all targets within the continuous viewing zone (CVZ) of 3 years of TESS 2 min cadence Simple Aperture Photometry (SAP) lightcurves, a description of which is provided by Jenkins et al. (2016). A total of 5535 year long lightcurves are searched for exoplanets with orbital periods in the range 1 – 100 days. Our search is complementary to the SPOC search for exoplanet candidates and any other searches of TESS 2 min data. The Planet-Hunters-TESS project (Eisner et al. 2020) identified a number of candidates in the first two-years of TESS 2 min data using a combination of visual inspection and semi-automated vetting. The Weird detector Wheeler & Kipping (2019); Chakraborty et al. (2020) was used to searched the first year of TESS data for any interesting periodic phenomena using a technique based on phase dispersion minimization. Additionally Wong et al. (2020) performed a phase curve study of the first year. TESS lightcurves have also been used to study stellar properties; an eclipsing binary (EB) catalog ⁶ produced by Prša et al. (2022) and Lund et al. (2021) process lightcurves to study asteroseismology.

Transit surveys operate with a high level of photometric sensitivity necessary to detect small changes in brightness caused by transiting exoplanets (Deeg & Alonso 2018). This also means that lightcurves constructed from aperture-summed pixels, are highly sensitive to changes in the pixel response function of a target. For example, instrument error may cause sub-pixel pointing offsets, or thermal broadening of the pixel response region, which is unaccounted for in aperture reduction. Sensor-wide noise effects which introduce correlated noise in lightcurves are termed systematics. The treatment of systematics is crucial in a transit pipeline, as systematics may conceal transit signals due to the magnitude and short timescale features of systematics.

Our detection method operates on lightcurves which contain unknown systematics, jointly modeling the various noise components and transits. A joint modelling approach is motivated by the difficulty in separating systematics from transit signatures with sequential processing, where detrending and detection are performed sequentially. Sequential processing may overfit and distort transit features (Christiansen et al. 2013; Foreman-Mackey et al. 2015) and consequently lower detection performance. Our joint detector computes a binary hypothesis test by marginalizing over an empirical systematics prior and stochastic noise prior given either hypothesis; a lightcurve contains a transit, or no transit. A benefit of the detector model is that it allows inherent uncertainty in systematic noise or stochastic noise to be averaged over with respect to a continuous range of models. The choice of prior weights the likelihood of these models. Our systematics model is low rank and consists of linear combinations of Cotrending Basis Vectors (CBV's) (Smith et al. 2012; Stumpe et al. 2012), with a Gaussian prior on the linear weights. A Gaussian prior is also used to model stochastic noise. The detector is closed form under the Gaussian noise assumption, and theoretically maximizes detection performance for a fixed rate of false alarm. The Systematics-Insensitive Periodogram (Hedges et al. 2020) is a Python tool to search TESS targets from the CVZ for long-period transit signals. This method uses a noise model which incorporates systematics, alongside sinusoid signal terms, which are jointly fitted to form a periodogram. A detector is different from a periodogram as a detector calculates a detection statistic which is calibrated by the likelihood of a null case, where no transit is present.

There are a number of major differences between the Kepler long-cadence data analysed in prior work and the TESS short-cadence data, which necessitate pipeline modifications from prior work. Approximately 13% of 2-minute flux measurements are missing or quality flagged. Within a single observational sector TESS undergoes two ~ 13.7 day orbits around the Earth (Stassun et al. 2018), between each ~ 13.7 day orbit data collection ceases for a few hours. Besides this periodic data gap, there are flagged and missing data due to a 2 – 6 day momentum dump cycle. Gap-filling is commonly used to handle missing data, and is requisite for use of Fourier-based methods such as a periodogram, however doing so may bias results and is challenging to do on large intervals. The detector used in this

⁴ tess.mit.edu/science/tess-input-catalogue/

⁵ tess.mit.edu/toi-releases/

⁶ <http://tessebs.villanova.edu/>

work is computed over non-uniform data where all missing or quality flagged cadences are excluded. We require 3 transit events to be present in the data for a transit detection.

A year-long lightcurve of 2 minute cadence observations consists of approximately $\sim 200,000$ data values, [Twicken et al. \(2019\)](#) describe computational challenges associated with this density of data. In order to achieve coverage of the space of detectable candidate transit signals detection tests are performed on 10^8 candidate transit models with a 10-minute step size in candidate period and epoch. The number of detection tests performed, as well as the complexity of each detection test, is polynomial with data-length. We efficiently implement the computation of many detection tests for this large space of candidate transit signals by exploiting similarities between transit signals of fixed duration in an approach similar to that used in [Jenkins et al. \(2010\)](#). Additionally our detector is broken down into sector-length computations. Our detector is implemented in a high performance computing architecture and achieves an overall linear-time complexity with data-length.

Differences in the form of noise and systematics in TESS data exist due to the differing mode of operations and telescope design. TESS data contains cadences of large short-term flux variations ([Nguyen et al. 2018](#)), sources include high pointing jitter, as well as flux ramps which occur before and after momentum dumps and sector downlinks. The joint noise model may capture harmonic noise and systematics, as such stitching of lightcurves via polynomial regression is not a requisite data processing step. However not all such instrumental noise is fully accounted for by the joint noise model or can be removed via masking. The periodic nature of noise and systematics are a significant source of false alarm detections. We filter false alarms using a robust metric derived for our detector and similar to [Seader et al. \(2013\)](#), alongside several other post-processing metrics.

We evaluate our theoretical detector performance via single-transit injection tests on a sample of 3000 lightcurves with limb-darkened transit signals described in Table 2.4.1. Our detector achieves a high detection efficiency of approximately 79% at a 19% quasi-false-alarm rate, defined as the rate of incorrect detection. The joint detector implementation does not provide a distinct performance benefit as compared to sequential detrending and detection for TESS data due to the nature of TESS systematics. In particular the form of TESS systematics are well constrained and relatively low magnitude, such that the benefit of marginalizing over a Bayesian prior is not seen here. In our full search of lightcurves from the CVZ for candidate exoplanets, approximately 28% of lightcurves have detections. Among these 77% of tess-objects-of-interest (TOI) present are recovered with a matching orbital period. A final list of 16 new candidate exoplanets is presented in Table 7, subject to stringent manual vetting to remove clear astrophysical false positives such as eclipsing binaries, as well as instrumental and statistical sources of false alarm.

The paper is organized as follows. Section 2 describes the the joint detector and implementation for TESS data. In Section 3 we report the results from our injection and detection results applied to TESS data. Section 4 contains a discussion of recovered candidates and conclusions are presented in Section 5.

2. METHODS

A Bayesian framework for detecting transits in SAP flux lightcurves which contain systematic noise was derived by [Taaki et al. \(2020\)](#), herein the scope is narrowed one such detector (described as 'Detector A') where systematic noise is modelled with a Bayesian prior which is marginalized over to compute a detection test. A concise overview of this detector in general form is described in Section 2.0.1.

2.0.1. Detection Model

A light curve \mathbf{y}_i for a particular star indexed by $i \in I$ (where I is the set of integers) is expressed as a vector of N photometric flux measurements in time, and hereinafter considered also to be normalized and median subtracted. The light curve vector \mathbf{y}_i is modelled as containing an unknown systematic noise signal \mathbf{l}_i and an unknown stochastic noise signal \mathbf{s}_i . For conciseness \mathbf{s}_i represents residual sources of non-systematic statistical error and stellar variability.

The transit detection framework is based on a binary hypothesis test: the null hypothesis (H_0) posits that \mathbf{y}_i contains no transit signal, the alternative hypothesis (H_1) posits that \mathbf{y}_i contains a transit signal $\mathbf{t} \in \mathbf{T}$, where the set \mathbf{T} describes all detectable transit signals. The detection test is therefore posed as:

$$H_0 : \mathbf{y}_i = \mathbf{s}_i + \mathbf{l}_i \quad (1)$$

$$H_1 : \mathbf{y}_i = \mathbf{t} + \mathbf{s}_i + \mathbf{l}_i \quad (2)$$

To decide between hypotheses in Equation 2 a likelihood ratio test (LRT) ([Kay 1993](#); [Wasserman 2013](#)) compares the probability of the raw light curve \mathbf{y}_i under either hypothesis model. If the LRT $\mathcal{L}_i(\mathbf{y}_i)$ exceeds a fixed threshold

τ then a transit signal has been detected. More generally we consider a test statistic $T(\mathbf{y}_i)$ obtained from simplifying the LRT, which is equivalent in detector performance to the LRT $\mathcal{L}_i(\mathbf{y}_i)$. Typically a Neyman-Pearson criterion (Kay 1993; Wasserman 2013), in which the probability of detection is maximized subject to a fixed rate of false alarm α , is used to decide the threshold τ . The detection test can be stated as:

$$T(\mathbf{y}_i) \equiv \mathcal{L}_i(\mathbf{y}_i) = \frac{p_1(\mathbf{y}_i)}{p_0(\mathbf{y}_i)} \underset{H_0}{\overset{H_1}{\gtrless}} \tau \quad (3)$$

where $p_h(\mathbf{y}_i) \equiv p(\mathbf{y}_i|H_h)$ is the probability of observing light curve \mathbf{y}_i under a particular hypothesis model $h \in \{0, 1\}$.

The systematics model is a low rank linear model with common basis vectors shared by a multiple targets on a sensor region and is of the form:

$$\mathbf{l}_i[n] = \sum_{k=1}^K c_k^i \mathbf{v}_k[n] \quad (4)$$

Where ($K \ll N$) describes the rank of the noise model and $\{\mathbf{v}_k : k \in K\}$ are a set basis vectors shared by lightcurves. Each c_k^i is a coefficient weighting of \mathbf{v}_k for lightcurve i . We denote the vector of coefficients for a lightcurve as $\mathbf{c}_i = [c_1^i, c_2^i, \dots, c_K^i]^T$, the set of coefficients for all lightcurves on a sensor is denoted as $\{\mathbf{c}_i : i \in I\}$.

The noise terms \mathbf{s} and \mathbf{l} are a-priori unknown but can be partially constrained by ancillary properties, hence we place probabilistic priors on the stochastic signal \mathbf{s}_i and systematic coefficients \mathbf{c}_i , and consider the exoplanet transit signal \mathbf{t} as deterministic but unknown. The chosen form of the prior distributions is Gaussian, $\mathbf{c}_i \sim \mathcal{N}(\mu_{\mathbf{c},i}, \text{Cov}_{\mathbf{c},i})$ and $\mathbf{s}_i \sim \mathcal{N}(\mathbf{0}, \text{Cov}_{\mathbf{s},i})$ motivated in Taaki et al. (2020) by the flexible modelling properties of Gaussians. Linear combinations of Gaussian distributions are Gaussian distributed, therefore the noise terms can be described by a single distribution $\mathbf{l}_i + \mathbf{c}_i \sim \mathcal{N}(\mu_{\mathbf{c},i}, \text{Cov}_{\mathbf{s},i} + \mathbf{V}\text{Cov}_{\mathbf{c},i}\mathbf{V}^T)$. The parameters of the models are based on empirical inference and described in Section 2.1.5 and Section 2.1.4.

The detection test can be defined under the joint Gaussian noise model as detection of a fixed signal \mathbf{t} in the presence of Gaussian noise $\mathbf{z}_i \sim \mathcal{N}(\mathbf{0}, \text{Cov}_{\mathbf{s},i} + \mathbf{V}\text{Cov}_{\mathbf{c},i}\mathbf{V}^T)$ within the shifted data $\hat{\mathbf{y}}_i = \mathbf{y}_i - \mathbf{V}\mu_{\mathbf{c},i}$. The matched filter is the Neyman-Pearson optimal detector for a fixed signal in Gaussian noise with test statistic $T_i(\hat{\mathbf{y}}_i)$:

$$T_i(\hat{\mathbf{y}}_i) = \frac{\hat{\mathbf{y}}_i^T \mathbf{C}_{\mathbf{z},i}^{-1} \mathbf{t}}{\sqrt{\mathbf{t}^T \mathbf{C}_{\mathbf{z},i}^{-1} \mathbf{t}}} \underset{H_0}{\overset{H_1}{\gtrless}} \tau \quad (5)$$

Exoplanet transits are searched for by computing transit detection tests $T_i(\hat{\mathbf{y}}_i)$ for a discretized set of candidate signals $\mathbf{t} \in \mathbf{T}$. The functional form of candidate transit signals, as well as the discretization of the search space are described in Section 2.1.2.

2.1. Implementation

The calculation of detection tests requires several stages of processing, admitting various choices for parameter estimation. A summary of the detector pipeline is shown in Figure 2. The detector implementation is tailored to the observing characteristics of the TESS telescope; in particular data gaps and noise properties are factors we consider in the estimation of noise priors, and the quantity of data necessitates efficient computation and management of detection data products. In Section 2.1.1 the chosen target lightcurves are described. In Section 2.1.2 the candidate transit search space is described. In Section 2.1.3 the nature of missing and quality-flagged TESS data is described along with it's treatment in our pipeline. The choice of estimation of stochastic and systematic noise priors is described in Section 2.1.5 and Section 2.1.4. A description of computational optimizations and requirements is provided in Section 2.3. The computation of the detector over all TESS observational sectors is described in Appendix A.

2.1.1. Target Lightcurves

The lightcurves selected for transit detection are from the first 3 years of TESS observations, and constitute all lightcurves from the CVZ⁷. Lightcurves were selected from this region as they have a high degree of data-completeness and allow for the detection of long-period signals. Years 1 and 3 are focused on the Northern hemisphere and hence

⁷ The continuous viewing zone (CVZ) is a region of the sky over which targets are continuously observed for the total year (13 sectors).

have some overlapping targets and year 2 the Southern hemisphere. In year 1 we search 1851 targets, year 2 2046 and in year 3 1922, the total number of unique targets is 5535. In Figure 1, the magnitude distribution of these targets for years 1, 2 and 3 is shown, TESS targets are relatively brighter than those surveyed by Kepler. We use short-cadence SAP lightcurves Jenkins et al. (2016) for which there is a 2 min integration time. A single year-long lightcurve has approximately 200,000 samples.

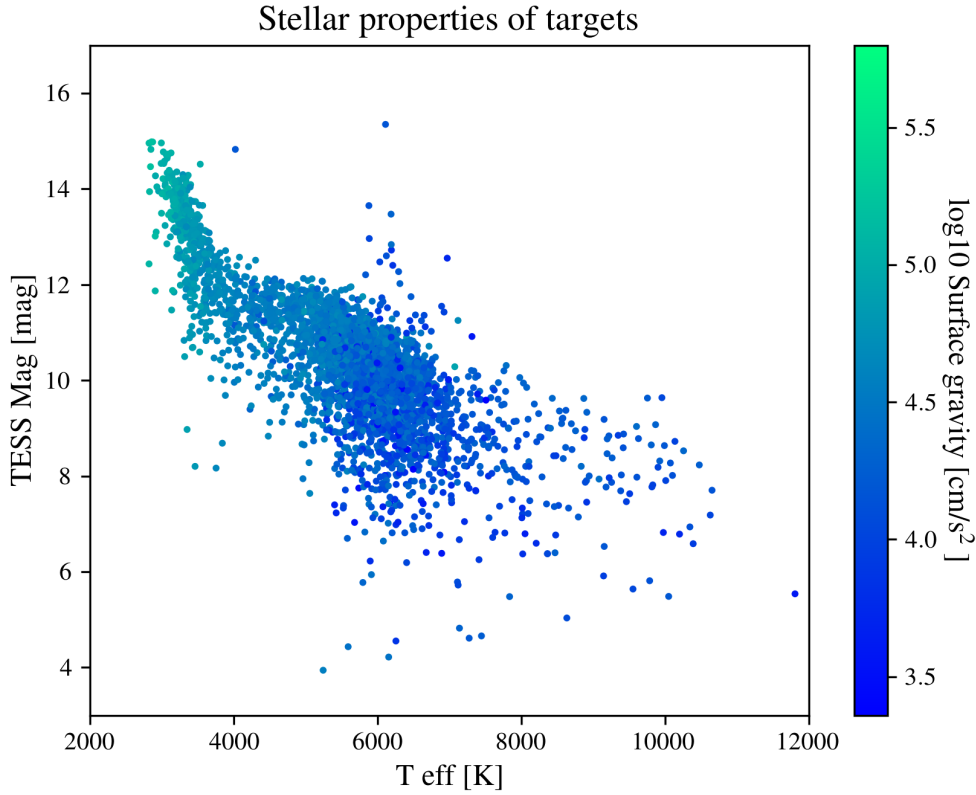


Figure 1. Stellar target properties. TESS targets constitute a bright sample of stars, with higher levels of stellar variability.

2.1.2. Transit Search Space

The objective of a transit search is to find any transit signal \mathbf{t} from the set of detectable transit signals \mathbf{T} which produce a detection test statistic above threshold. Typical parametric models for a transit signal \mathbf{t} include limb-darkening models (Mandel & Agol 2002), or box-functions, however such models cannot simply or analytically be solved for candidate transits which exceed the detection threshold. Instead a discrete space of candidate transits is constructed broken down by period P , epoch e and duration d , over which detection tests are performed. Herein \mathbf{t} is approximated as a box function described by Equation 6, with a search space in Table 1. Any candidate signals which do not have 3 transits present in the data (each transit occurring on a minimum of one non-masked cadence) are removed from this search.

$$t_{\alpha,P,e,d}[n] = \begin{cases} \alpha, & \text{if } (n - e) \bmod P \leq d \\ 0, & \text{otherwise} \end{cases} \quad (6)$$

For a matched filter based detector, the detection error due to mismatch between the box transit shape and true astrophysical transit shape is generally very small (Van Trees 2001; Seader et al. 2013). However this also means that the detection test can produce false-alarm detections for outlier signals such as flares or sudden pixel sensitivity

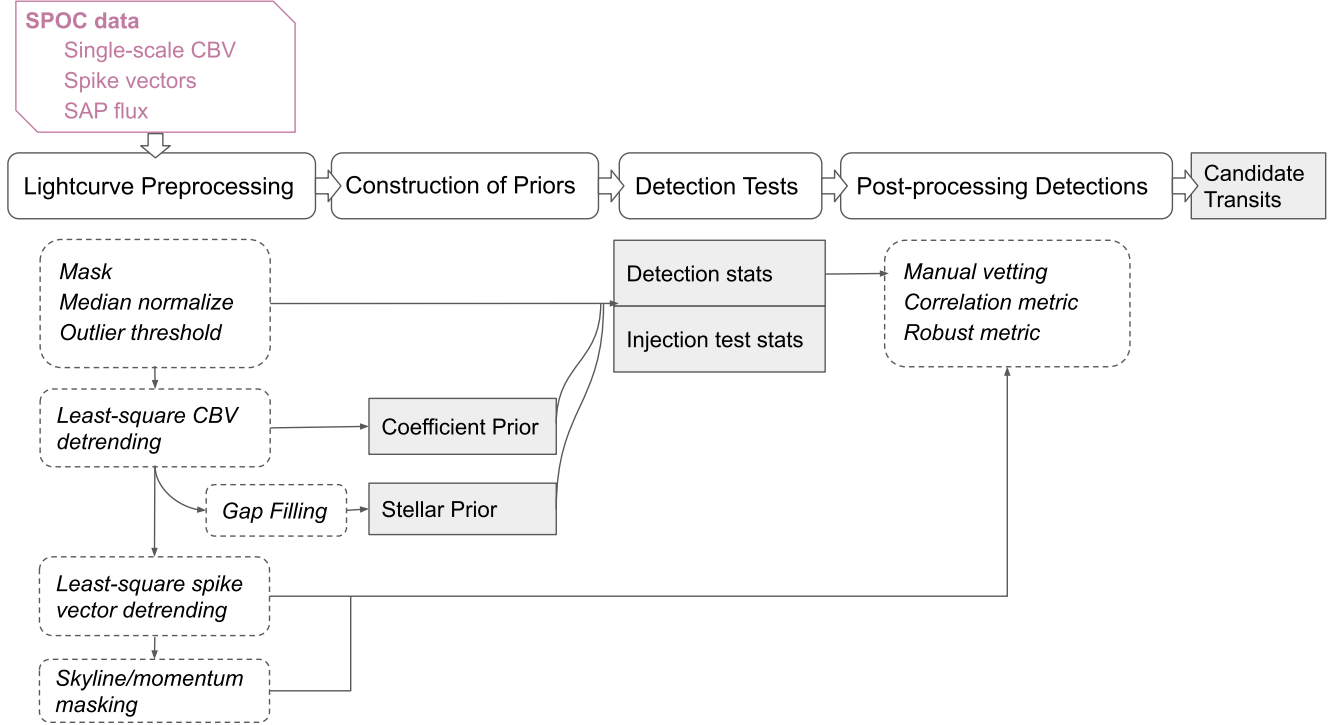


Figure 2. A schematic of the pipeline. Data input from SPOC are shown in pink. Processing steps are shown in rounded edge boxes, with major processing steps shown with a solid outline and component processing steps dashed. Beneath each major processing step are the corresponding component processing steps, and any data output in grey filled boxes.

dropouts which are not otherwise included in the noise model and are close in form to a transit signal. As such we introduce post-processing filtering which is described in Section 2.2.1.

Table 1. Transit Search Space

| Transit Parameter | Range | Step Size |
|-------------------|--|-------------------------------|
| Orbital period | $P \in [1, 100]$ d | $\delta P \in \{10, 20\}$ min |
| Transit duration | $d \in \{1, 2, 3, 4, 6, 8, 10, 12, 14, 16\}$ h | |
| Epoch | $e \in [0, P]$ | $\delta e \in \{10, 20\}$ min |

NOTE—The sample integration time is $\Delta t_{LC} = 2$ min. The step size of period δP and epoch δe is 10 min for candidate periods less than the length of a sector ~ 27 days, otherwise δP and δe are 20 min.

For a year of data, we evaluate approximately $|\mathbf{T}| \sim 2 \times 10^8$ candidate transit signals per lightcurve. As described in Jenkins et al. (2010), the epoch and period step size should be chosen to afford a high level of correlation between a single transit event and a candidate signal. However, even with a high degree of precision for single transit signal matching, there is still the possibility for significant mismatch for the full length candidate transit. The maximum error in P is half the step size: $\frac{\delta P}{2}$. Among all candidate transit signals of the same period, the epoch which minimizes the worst-case single transit offset is that which provides the best match for (approximately) the middle transit event. In which case the worst case offset of a single event is approximately the number of transits that occur in half of the lightcurve $\frac{N}{2P}$ multiplied by the maximum error in period $\frac{\delta P}{2}$ as: $\frac{N}{2P} \cdot \frac{\delta P}{2} = \frac{N\delta P}{4P}$. For example, a transit signal with period $P = 8$ days can incur an approximate worst case error in the location of a single transit event of ~ 2 h, if the transit duration is less than 2 h the template and transit event may be entirely mismatched. To account for mismatch

when calculating the matched filter test in Equation A2, the candidate transit restricted to a sector for a fixed period and epoch, is allowed to shift ± 2 h in epoch and find the maximum detection statistic within this window.

2.1.3. Lightcurve Pre-processing

A primary issue of TESS data as compared to Kepler data is the quantity and cadence of missing data, particularly posing a challenge the detection of long-period signals (Hedges et al. 2020). Approximately 9% of TESS data is missing, and a further 4% of cadences are marked by quality flags. The majority of missing data occurs due to a 3 – 6 day momentum dump cycle and a day-long downlink that occurs every ~ 13.7 days. In Figure 3 the average fraction of missing data/quality flagged data for the target lightcurves is shown per sector. Figure 5 shows the average density of missing data for the target lightcurves over time, each pixel represents a day and the color represents the density of missing data. Due to the largely periodic nature of the data-gaps a large number of candidate transit signals will have transits occurring on data gaps reducing the overall detection completeness.

The use of gap-filling in the data-processing pipeline can bias results since the data admits a significant fraction of missing cadences. Furthermore, it is challenging to do so without introducing spurious discontinuities due to flux ramp systematics occurring before and after data gaps. Our detector described in Equation A2 does not require any gap filling and can be directly applied to non-uniform data. In computing detection tests, we excluded all missing and quality-flagged cadences. Not all data marked by a quality-flag should necessarily be excluded, however the TESS handbook states the following flags are of lower quality [1,2,4,8,16,32,128,512,4096]. In Figure 4 the distribution of different quality flags in the data is plotted, the majority of flagged data falls under one of the lower quality flags.

Although the detector does not require uniform data, estimating the noise priors using traditional techniques is challenging since many are not designed to handle non-uniform data. In particular two challenges arise: i) the excluded cadences may not be the same between lightcurves and the use of principle component analysis (PCA) or the singular value decomposition (SVD) (Cunningham & Ghahramani 2015) to estimate a systematic basis requires complete data, ii) Fourier-based spectral methods which may be used for stochastic noise estimation or phase correlation, as described in (Taaki et al. 2020), require uniform data. Our chosen empirical estimation method for the stochastic covariance Cov_{s_i} (the stochastic covariance for a particular lightcurve, and a particular sector) utilizes some gap filling in order to use the Fourier based smoothed periodogram described in Section 2.1.5. Gap-filling was performed by selecting a random portion of the lightcurve from the same sector to fill each gap. There is room for improved methods here, capable of removing transit-like harmonics while capturing periodic stellar fluctuations. A standard sample covariance would not require any gap-filling, however such an estimate is not robust to inclusion of signals of interest.

2.1.4. Systematic Prior

The basis set $\{\mathbf{v}_k : k \in K\}$ is generally estimated based on the collection of lightcurves using a linear low rank decomposition. In this implementation the TESS single-scale cotrending basis vectors (CBV) (Smith et al. 2012; Stumpe et al. 2012) are used as a basis set $\{\mathbf{v}_k : k \in K\}$. Per sector, per ccd/camera pair there is an independent set of CBV's, there are between 16 and 8 CBV's available for a given set, an example set is shown in Figure 6. We note that systematic flux ramps occurring before and after data downlinks (midway and at the end of a sector) are not included in the CBV's, and we did not detrend them, the effect of which is described in further detail in the results Section 3.

Provided the size of the basis set is small relative to the number of lightcurves $K \ll |I|$, the estimation of $\{\mathbf{v}_k\}$ is well-conditioned. On the other hand, a least-squares fit of this basis to a single lightcurve, without prior knowledge of a transit, may overfit and distort transits (Smith et al. 2012; Stumpe et al. 2012). A prior $p(c_i)$ may improve systematics estimation by restricting the coefficient values based on the properties of systematics observed in the overall collection of lightcurves. As in prior work we form a model of the covariance of coefficient vectors Cov_c based on the sample covariance formed from least-square fits using all available (masked) lightcurves for the sector/camera/CCD combination. Although each individual least-square fit may be susceptible to overfitting to astrophysical signals, since astrophysical signals may be fairly assumed independent, the sample statistics are assumed to be approximately unbiased. In Figure 7 a histogram of the leading basis term coefficient fits is shown with a Gaussian fit overlaid. The mean coefficient vector μ_c is chosen as the least squares fit for the lightcurve under consideration.

2.1.5. Stochastic Prior

The Gaussian noise model of the form $\mathbf{s} \sim \mathcal{N}(0, \text{Cov}_s)$ is a stochastic model of the observed stellar variability in addition to readout error and Poisson noise on the source and sky count (Ronald L. Gilliland et al. 2011), under the

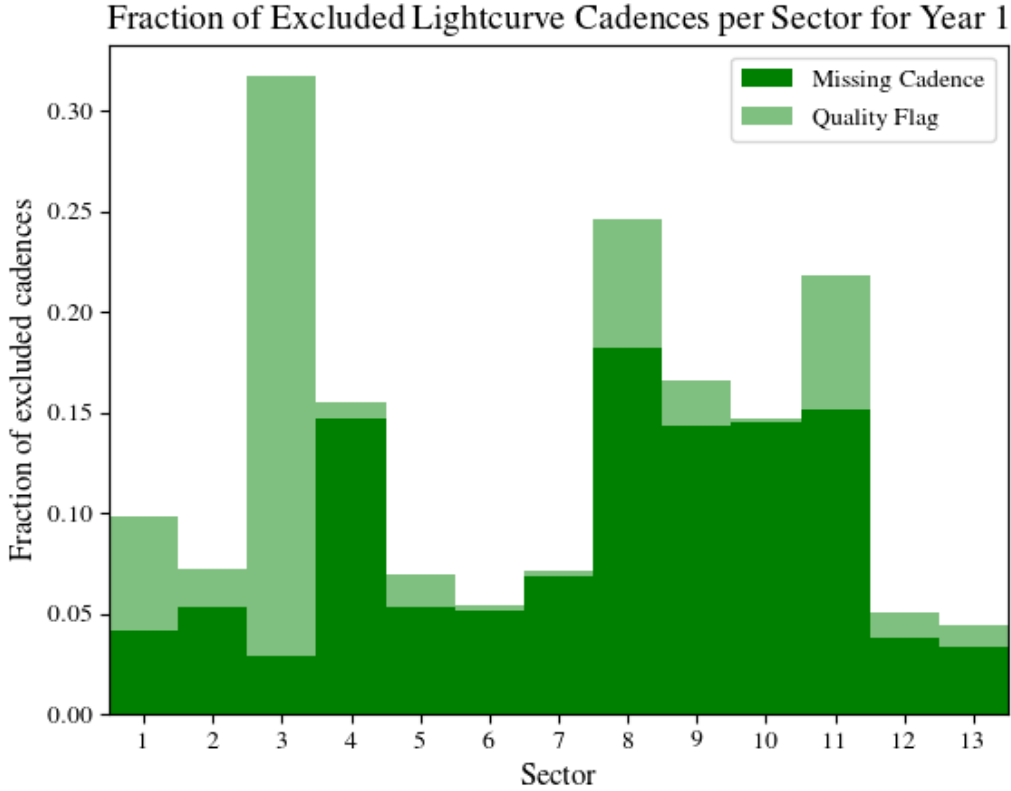


Figure 3. The average fraction of missing data/quality flagged data for the target lightcurves is shown per sector for year 1 lightcurves. A large fraction of data is missing, and a relatively smaller fraction is quality flagged.

central limit theorem the sum of these individual sources is approximately Gaussian. The stochastic noise model is completely described by the covariance $\text{Cov}_s \in \mathcal{R}^{N \times N}$ which describes the dependence between points in time.

A model of Cov_s is required for the detector in Equation 5. Stellar variability may exhibit harmonic structure, stellar rotation and activity/starspot regions alongside short-term correlated noise. Physically motivated covariance models have been sought for detailed modelling of stellar activity e.g. [Angus et al. \(2017\)](#), and [Rasmussen \(2003\)](#) for a description of parametric covariance models. In this implementation we use a non-parametric estimator based on empirical fits, however restrict the form to be stationary ($\text{Cov}(t, s) = f(|t - s|)$) per sector. The stationarity assumption reduces the number of variables to estimate providing robustness to non-Gaussian signals. It is not a necessary requirement for the detector, neither does it provide any computational benefit. In the SPOC pipeline the median-absolute-deviation is used to estimate the local noise level, this approach allows for more precision and is appropriate where noise statistics are highly variable but is susceptible to inclusion of transit signals ([Seader et al. 2013](#)).

For a particular lightcurve, and sector we estimate Cov_s using least-square detrended and 3σ outlier thresholded lightcurves. The stochastic covariance Cov_s should capture harmonics and correlations, but be generally insensitive to transit features. The sample autocorrelation for a lag k averaging over $(N - k)$ samples, is approximate χ_k^2 distributed. For larger lags for which there are less data-samples, an estimate $\text{Cov}_s[t, s] : |t - s| = k$ is subject to greater estimation variance. We use the smoothed periodogram which has the effect of frequency binning and suppresses the covariance at large lag values. In Figure 8 an example spectrum is shown. In Figure 9 an example of a lightcurve and the associated covariance estimate is shown and compared to the sample autocovariance, which can be seen to include transit correlations. Since lightcurve data is non-uniform, segments of data are used to impute gaps to compute the spectral estimate. We emphasize the chosen covariance estimator is not necessarily optimal, nor requisite.

2.2. Post-processing

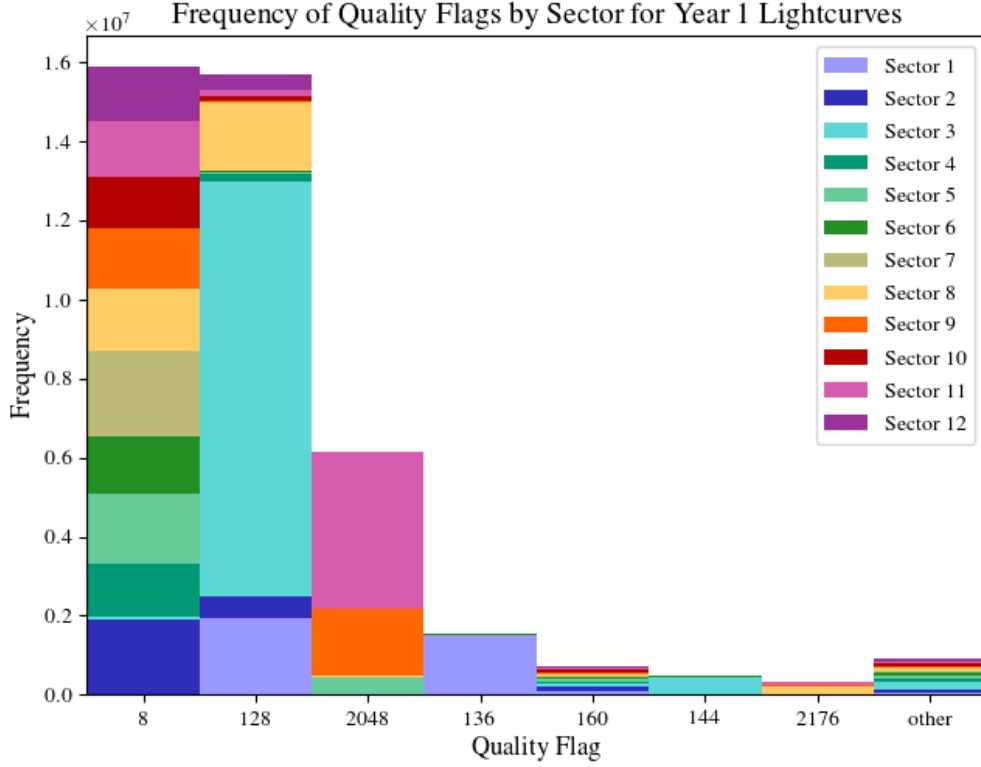


Figure 4. The frequency of quality flagged cadences as they occur in lightcurves. The most commonly occurring quality flags are; Key: 8-Spacecraft is in Earth Point, 128-Manual Exclude due to an anomaly, 2048-Stray light from Earth to Moon in Camera FOV.

Among detected transits a variety of false alarms are present, where possible we introduce post-processing metrics to filter them. These metrics are informed by the Kepler and TESS science processing. Stochastic noise may incidentally correlated with a candidate transit \mathbf{t} , thus the transit detection model described in Section A incurs a theoretical rate of false alarm over the space of candidate transit signals \mathbf{T} denoted as P_{FA} ⁸. The probability of no false alarms is non-increasing with the number of candidate transits evaluated $|\mathbf{T}|$, however we find that due to the form of the candidate transits, the asymptotic P_{FA} does not depend on $|\mathbf{T}|$ and is approximately constant. This is due to the large degree of correlation among the candidate transits $\mathbf{t} \in \mathbf{T}$.

Consider that each detection test for $\mathbf{t} \in \mathbf{T}$ can be viewed as an inner product with a vector $\mathbf{m}(\mathbf{t})$ determined by the candidate transit \mathbf{t} and the lightcurve \mathbf{y} . For there to be no false alarm for a candidate transit \mathbf{t} the detection test must be below a threshold τ : $\mathbf{y}^T \mathbf{m}(\mathbf{t}) \leq \tau$. For this condition to be satisfied \mathbf{y} must belong to a halfspace determined by the line tangent to the vector $\tau \frac{\mathbf{m}(\mathbf{t})}{\|\mathbf{m}(\mathbf{t})\|}$. For there to be no false alarms for all $\mathbf{t} \in \mathbf{T}$, \mathbf{y} must belong to the intersection of all halfspaces generated by \mathbf{T} . Since the area of the intersection of halfspaces is non-increasing with the size $|\mathbf{T}|$ and with τ , the probability of false alarm is non-decreasing.

$$P_{FA} = 1 - P_0\left(\bigcap_{\mathbf{t} \in \mathbf{T}} \mathbf{y}^T \mathbf{m}(\mathbf{t}) \leq \tau\right) \quad (7)$$

To calculate P_{FA} we use the simplifying approximation that lightcurve noise is white-noise $\mathbf{y}|H_0 \sim \mathcal{N}(0, I)$, such that $\mathbf{m}(\mathbf{t}) = \frac{\mathbf{t}}{\sqrt{\mathbf{t}^T \mathbf{t}}}$ and is unity-length $\|\mathbf{m}(\mathbf{t})\| = 1$. Denote the polytope generated as the intersection of halfspaces

⁸ Here the theoretical false alarm rate is typically referred to as the family-wise error rate.

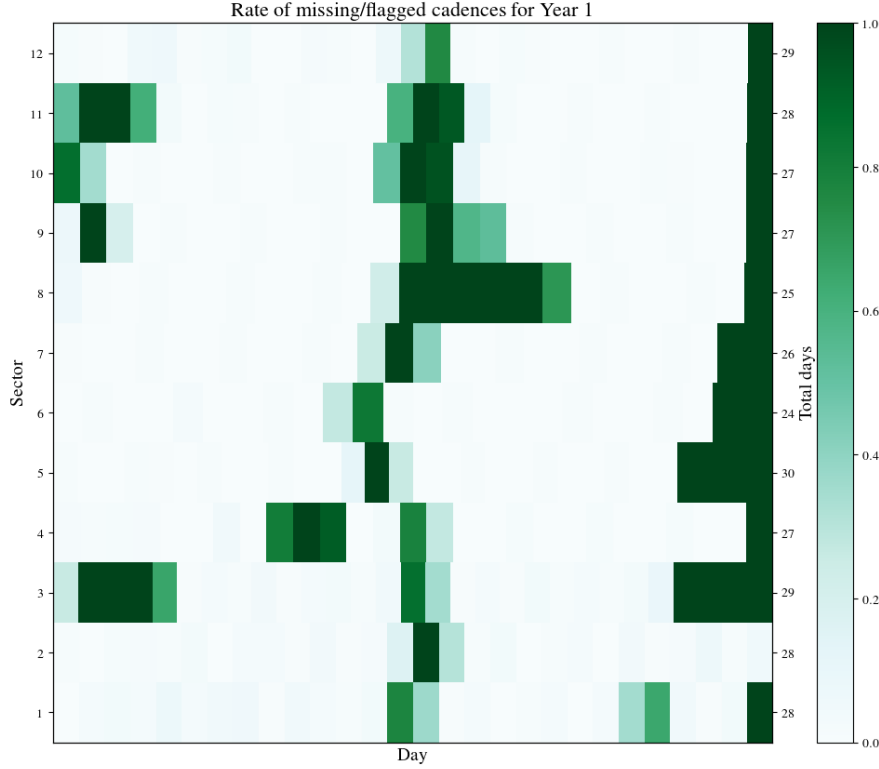


Figure 5. The rate of missing data, shown averaged over each day of data throughout year 1 and over all lightcurves. Each row represents a sector of data, sectors are variable length, the total number of days in a sector is displayed on the right ticks. Each block represents the average fraction of data excluded (due to a quality flag or missing cadence) among the selected lightcurves, averaged over a day (approximately 720 cadences). Over each 28 day sector, most missing data occurs at the mid-point due to a data downlink. However missing data also occurs throughout the remaining observational window.

tangent to $\tau \mathbf{m}(\mathbf{t})$ as A_{NFA} . For a length N vector there are 2^N orthants of the space which the vectors \mathbf{y} and $\mathbf{m}(\mathbf{t})$ are defined over. All vectors \mathbf{t} and consequently $\mathbf{m}(\mathbf{t})$ always lie in the negative orthant, therefore the positive orthant is always completely included in A_{NFA} . The N dimensional circle of radius τ , restricted to the negative orthant, is always contained in A_{NFA} . This circular shape is generated by \mathbf{t} which uniformly span the negative orthant. All orthants not specified, have the region below τ along one axis in A_{NFA} . Integrating the probability over A_{NFA} we obtain:

$$P_{FA} \leq 1 - \frac{1}{2^N} - \frac{1}{2^N} P_0(\|\mathbf{y}\| \leq \tau) - \frac{2^N - 2}{2^N} P_0(\|\mathbf{y}[i]\| \leq \tau) \quad (8)$$

The distribution of $\|\mathbf{y}\| \sim \chi(N)$ such that $P_0(\|\mathbf{y}\| \leq \tau) = \mathcal{P}(\frac{N}{2}, \frac{\tau^2}{2})$ where \mathcal{P} is a regularized Gamma function. A single sample $\mathbf{y}[i]$ is normally distributed, and $P_0(\|\mathbf{y}[i]\| \leq \tau) = Q(\tau) - Q(-\tau)$. Practically for N considered here, the contribution of the positive and negative orthant is negligible. This implies for large enough N the probability of false alarm $P_{FA} \leq 1 - (Q(\tau) - Q(-\tau))$, this implies performing more detection tests at a finer discretization will not significantly increase the rate of false alarms.

The theoretical false alarm rate is the contribution to false alarms due to Gaussian noise, however in practise the major source of false alarms are from signals which are non-Gaussian and therefore not included in the hypothesis

TESS Cotrending Basis Vectors 8/16 (Sector: 2, Cam: 4, CCD: 3)

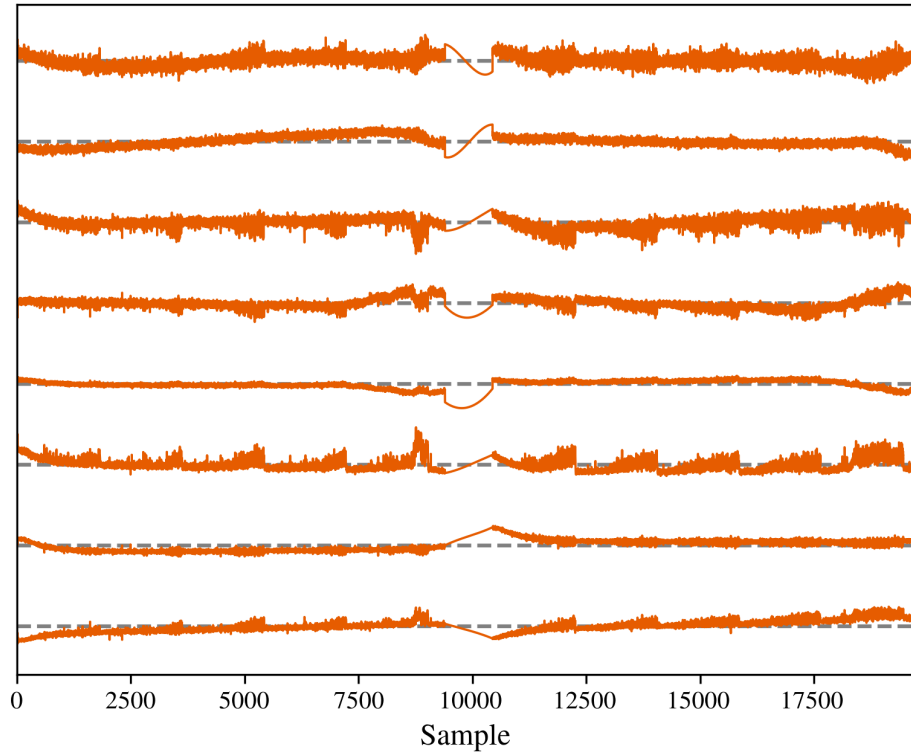


Figure 6. A sample of 8/16 cotrending basis vectors (CBV) are shown at a 2 min cadence. The CBV's capture systematics induced by the TESS sensor, in particular the 3 – 6 day momentum dump cycle causes periodic flux ramps.

model. In particular outlier noise and unmodeled systematics, for further details see Section 3.1. Outlier noise⁹ not appropriately modeled as Gaussian noise can produce false alarms (Seader et al. 2013), in particular producing strong detection statistics for long-period candidate transit signals (Twicken et al. 2016). Negative noise over a transit-scale interval has the maximal contribution to a detection test statistic among all candidate transits, for a transit with minimal number of transit events. In our pipeline processing, the use of CBV's without further filtering was found to produce false alarms due to unmodelled systematics occurring at data-downlink times and producing instances of negative noise. In addition to these sources of false alarm, eclipsing binaries and stellar harmonics are known to mimic transit signals and induce spurious detections. Below we describe several metrics to filter spurious false alarms.

2.2.1. Robust Statistic

A Chi-squared statistic (Seader et al. 2013) is used in the SPOC pipeline to filter false-alarms. We construct a similar metric based on the deviation of observed detection statistics per transit event, from the theoretical distribution. In particular, a true transit signal should be of relatively consistent depth across all in-transit events, whereas outlier or systematic contributions are not restricted to produce consistent depths.

The detector described in Section 2.0.1 is itself a random variable since \mathbf{y}_i is stochastic. A candidate transit signal \mathbf{t} may be decomposed as the sum of single transit event vectors which are zero except on the interval of the location of the transit event. Consider computing a generalized detection test in Equation 5 for a single transit event denoted

⁹ We define outlier noise as non-correlated noise of relatively large magnitude, short duration and not repeated throughout the lightcurve, either of astrophysical or instrumental origin.

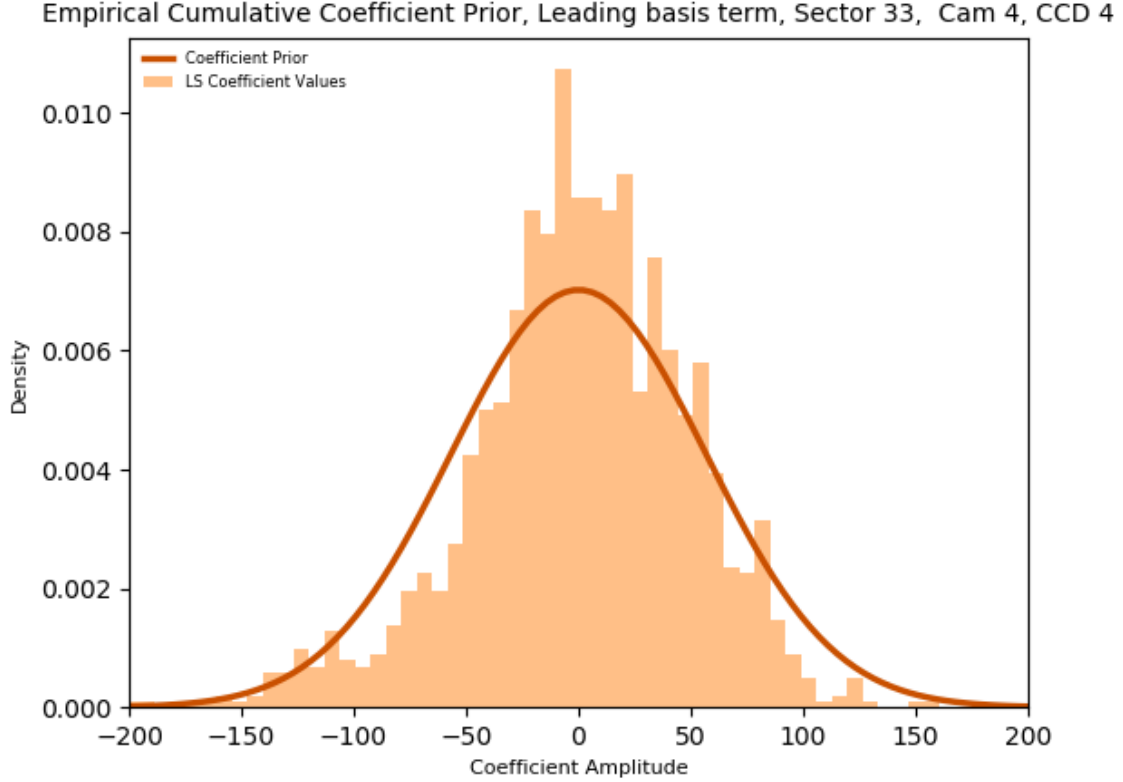


Figure 7. Gaussian fit of of empirical least-square fits for the leading basis vector, demonstrates approximate Gaussianity of the samples.

by \mathbf{t}_o . Under either hypothesis the detector is Gaussian distributed with the following statistics:

$$T(\mathbf{y}_i)|_0 \sim \mathcal{N}(0, 1) \quad (9)$$

$$T(\mathbf{y}_i)|_1 \sim \mathcal{N}(\alpha \cdot \sqrt{\mathbf{t}_s^T \text{Cov}_z^{-1} \mathbf{t}_s}, 1) \quad (10)$$

Where α represents the unknown signal to noise strength under the alternate hypothesis.

If the a scaled candidate transit is present in the lightcurve, the single event statistics should theoretically be Gaussian distributed with variance 1 about $\alpha \cdot m_s$, with $m_s = \sqrt{\mathbf{t}_s^T \text{Cov}_z^{-1} \mathbf{t}_s}$. Allowing the unknown scaling $\alpha \geq 0$, both the null and alternate hypothesis may be described by this same distribution. The negative \ln likelihood of the computed single event statistics given this theoretical distribution is equivalent to as a likelihood test:

$$-\ln \left(\mathcal{L} \left(\prod_s T_i(\mathbf{y}_i) = \alpha \cdot m_s \right) \right) \propto \frac{1}{N_s} \sum_s^{N_s} (T_i(\mathbf{y}_i) - \alpha \cdot m_s)^2 \quad (11)$$

A-priori the approximate signal strength α is unknown. The false alarms caused by outlier signals in this search tended to constitute a small fraction of spurious outlier events, alongside a larger fraction of either real transit events or null events. Hence the sample median of $\{\frac{T_s}{m_s}\}$ is an appropriate estimator of α , as it is robust to outlier values and equivalent to the sample mean under the theoretical Gaussian distribution.

The offset statistic $T_i(\mathbf{y}_i) - \alpha \cdot m_s$ has a standard normal distribution. Under the lightcurve model in Equation 2, the scaled sum of these variables in Equation 11 is theoretically χ^2 with an expected value of 1. A lower value of the negative likelihood indicates that the lightcurve is well-described by the hypothesis model. However the metric will be larger than it's theoretical distribution due to: i) inherent inaccuracy in estimating the noise and ii) the search

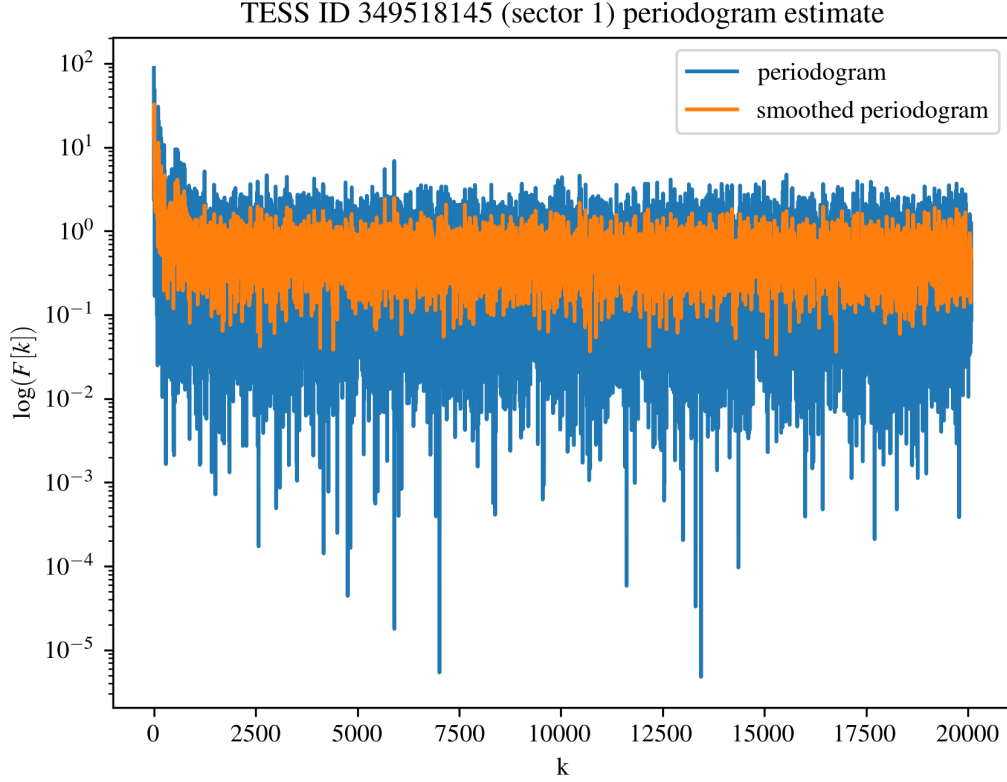


Figure 8. Periodogram and smoothed periodogram with smoothing window $K = 3$. This estimator of the stellar spectrum suppresses strong harmonics and can therefore provide some robustness to unfiltered transit signals.

space discretization will cause varying levels of match between candidate transit and true transit. In particular shorter duration transits will be subject to greater mismatch error.

This statistic was practically used to filter long-period signals with less than 5 transits, we remove approximately 50% of detected transits with variance > 1.5 .

2.2.2. Correlation Statistic

Alongside the robust statistics we compute the correlation coefficient between the identified transit signal \mathbf{t} and a processed lightcurve $\mathbf{y}'_i : \frac{\mathbf{t}^T \mathbf{y}_i}{\|\mathbf{t}\| \|\mathbf{y}_i\|}$. The correlation coefficient is computed on lightcurves which have been least-square cotrended with cotrending basis vectors, alongside spike vectors, produced by the SPOC pipeline (Jenkins et al. 2016). The correlation coefficient is computed with a window tolerance about the expected location of a transit event as described in Section 2.1.2.

In addition to the masking applied to the lightcurves described in Section 2.1.3, further masking is applied to the lightcurves used to compute the correlation coefficient. Masking is applied to cadences occurring -1 h of momentum dump times and cadences with unmodeled systematics which excessively contribute to detection statistics in multiple lightcurves. Figure 10 illustrates an instance of this occurring using the results from the TESS search, there is an increased density of transit events associated with unmodeled systematic scatter. These cadences are obtained from a histogram of the cadences occurring in transit events for all detections, for all lightcurves within a year. Approximately 1000 – 3000 of cadences on which detections are densest are masked. This metric is termed a skyline histogram and originates from the TESS-ExoClass project ¹⁰. Figure 10 illustrates a skyline plot for Year 3 data, for which 500 cadences are filtered.

¹⁰ github.com/christopherburke/TESS-ExoClass

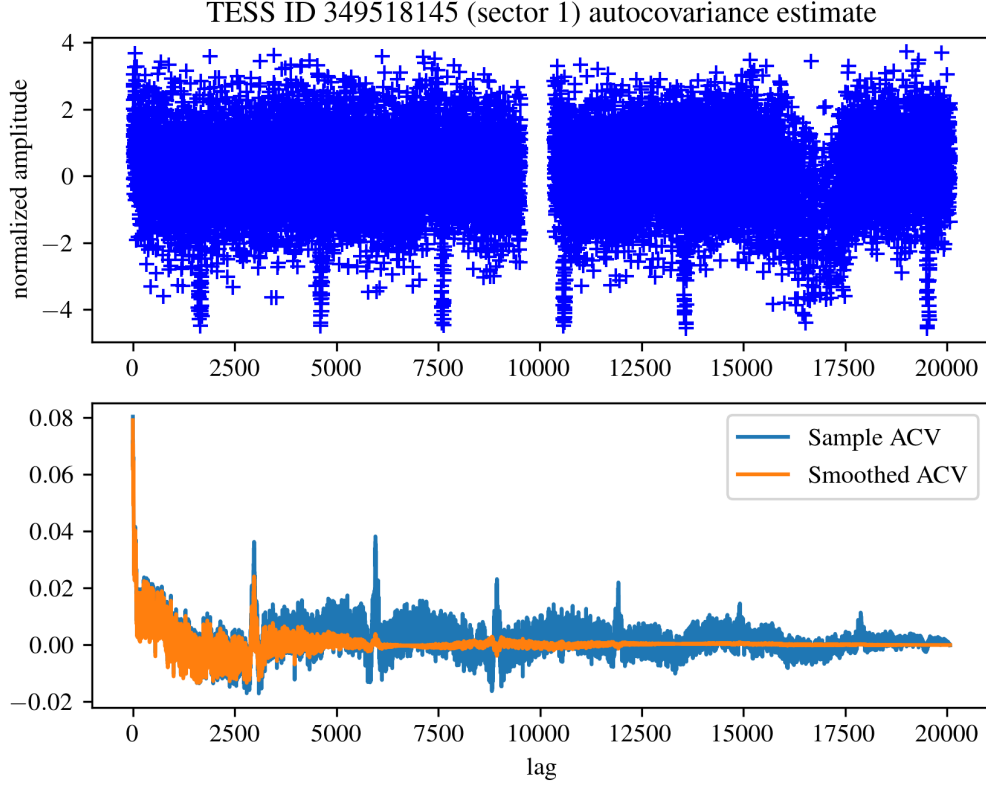


Figure 9. Even with thresholding, sometimes residual transit signals remain and can distort stellar covariance estimates as can be seen from the peaks, leading to missed detections. The smoothed estimator suppresses the covariance at larger lags.

The correlation metric is used as a heuristic to threshold filter approximately ($\frac{1}{3}$) of lightcurves with detections. The correlation is used as a coarse heuristic to filter clear cases where a detected transit is correlated with systematics or noise.

2.2.3. *Eclipsing Binaries*

In addition to false alarms produced by spurious systematics or statistical noise, false positives are incurred by transit dips produced by eclipsing binaries [Santerne et al. \(2013\)](#). A catalog ¹¹ of candidate eclipsing binaries found in the first two years of TESS lightcurves was produced by [\(Prša et al. 2022\)](#). In vetting candidate exoplanets we consider if the target has been designated as a candidate eclipsing binary, however as they are unconfirmed in certain cases the signal is a plausible exoplanet. A total of 99 of our targets are marked as candidate eclipsing binaries. Alongside the EB catalog, we produce even-odd phase folded lightcurves to identify eclipsing binaries. If the depth of even and odd transits is not the same, it is likely the transit events are produced by binary eclipsing stars.

2.3. *Computational methods and complexity*

This section characterizes the computation of detection tests in the schematic of the pipeline in Figure 2. This project was completed with 250,000 node hour allocation, with 32 core hours per node hour on the Blue Waters petascale system. Per year of lightcurve data detection tests required $\sim 50,000$ node hours, with 50 TB of intermediate storage required.

2.3.1. *Efficient computation of many transit detection tests*

¹¹ tessebs.villanova.edu

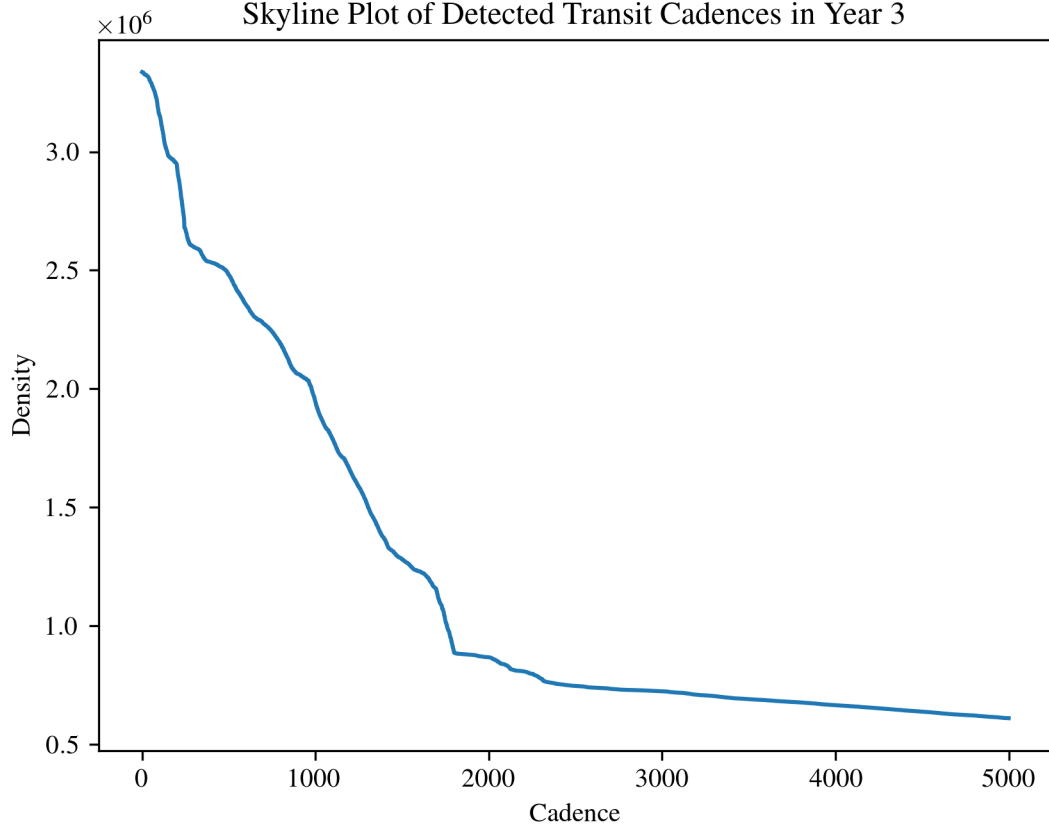


Figure 10. Sorted histogram of cadences contributing to detected transit events for Year 3. The sharp knee is used to threshold filter the cadences which contribute most significantly to detections over the collection of lightcurves.

The inverse covariance calculations $\text{Cov}_{\mathbf{z}}^{-1}$ are not a significant part of the pipeline computations as they only need to be performed once per lightcurve since the covariance is independent of the transit \mathbf{t} under study. The detector involves the computation of a matrix-vector product $\text{Cov}_{\mathbf{z}}^{-1}\mathbf{t}$ of $O(N^2)$ which is reused in the numerator and denominator of a transit detection test. We efficiently implement the computation of many of these calculations for a large number of candidate transit signals $\mathbf{t} \in \mathbf{T}$ by exploiting similarities between transit signals of fixed duration d , a similar approach is described in (Jenkins et al. 2010). Candidate transit signals are represented by a signal that is zero everywhere except on disjoint in-transit cadences. As such a candidate transit signal may be decomposed into a number of disjoint single transit events. The computation $\text{Cov}_{\mathbf{z}}^{-1}\mathbf{t}$ can be decomposed into the sum of matrix vector products of $\text{Cov}_{\mathbf{z}}^{-1}$ with single transit events comprising \mathbf{t} . The matrix-vector product of $\text{Cov}_{\mathbf{z}}^{-1}$ with a single transit event can then be efficiently computed, since the entries of $\text{Cov}_{\mathbf{z}}^{-1}$ needed for this computation represent a contiguous slice of matrix columns in memory, the d columns of length N are then summed to produce a length N vector, hence this computation consists of dN additions. These calculated vectors for single transit events are stored to compute detection tests for a range of candidate transit signals of fixed transit duration d , hence performing dN adds $\frac{N}{\delta e}$ times, therefore to compute the single transit calculations for fixed duration d requires $\frac{N^2 d}{\delta e}$ additions. Computing these values for all candidate durations D therefore requires $\sum_{d \in D} \frac{N^2 d}{\delta e}$ additions.

Denote the average number of transit events for $\mathbf{t} \in \mathbf{T}$ as $\mu_{\mathbf{t}}$. Matrix-vector products $\text{Cov}_{\mathbf{z}}^{-1}\mathbf{t}$ on average require the addition of $\mu_{\mathbf{t}}$ single transit vectors of length N per transit. Therefore requiring $|\mathbf{T}|N\mu_{\mathbf{t}}$ additions for transit search space \mathbf{T} . The average number of transit events $\mu_{\mathbf{t}}$ in a transit signal \mathbf{t} is found as a constant factor, see Appendix section B for this calculation.

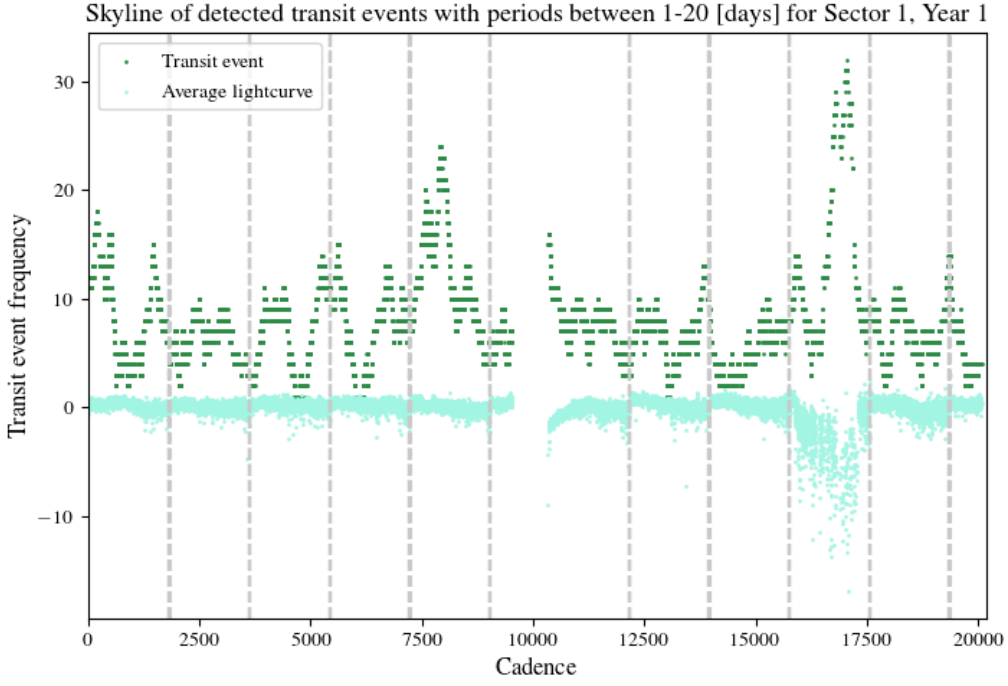


Figure 11. A skyline plot of detected transits from the TESS search with periods between 1 – 20 days shown for sector 1. The gray dashed lines indicate the occurrence of a momentum dump. The points marked as 'transit event' indicate the frequency of that cadence occurring in detected transit events (among the output detections where there is not more than one per target). The average lightcurve is a unitless lightcurve produced as the average of detrended and masked lightcurves among the targets with detected transits. Between cadences 16000 – 17500 significant scatter is left in the lightcurve (uncorrected by systematics) which produces a higher density of detected transit events. However overall the density of detections in this period range is not attributable to a singular systematic source.

A final detection test for a single candidate transit \mathbf{t} requires inner product calculations of $\text{Cov}_{\mathbf{z}}^{-1}\mathbf{t}$ with \mathbf{y} in the numerator, and \mathbf{t} in the denominator. This requires N multiplications and additions respectively. The transit search of \mathbf{T} for a single lightcurve is of complexity $O(|\mathbf{T}|N(1 + \mu_t) + \frac{\sum_{d \in \mathcal{D}} dN^2}{\delta_e})$. The size of the transit-search space $|\mathbf{T}| \gg N$, therefore we can drop the last term in the complexity. Since μ_t is constant factor, the complexity is therefore $O(|\mathbf{T}|N)$.

2.3.2. High-performance-computing pipeline

Lightcurve SAP data as provided by the MAST archive is broken down per lightcurve, per sector of data. Each file is of size 2 MB, a year of data for lightcurves from the continuous viewing zone occupies ~ 50 GB in hard disk. Computations as described in Section 2.3.1 are performed per sector, before combined as in Equation A3 to compute a detection tests for each lightcurve, over the set of transits \mathbf{T} for a full year. Computations described in this section, are independent between lightcurves, and furthermore between candidate transit durations. We describe the pipeline to implement the computation of detection tests for a year-long lightcurve on the Blue Waters petascale system (Mendes et al. 2015) with full node utilization, and the associated computational requirements.

In the first step, per lightcurve, per sector, the inverse covariance $\text{Cov}_{\mathbf{z}_i(q)}^{-1}$ of size $N_q \times N_q$ is computed once per lightcurve. This matrix is ~ 1.7 GB and stored on hard disk, to store covariances for all sectors (13) within a year requires 22 GB per lightcurve. For all lightcurves in the CVZ of a single year requires approximately 35 TB.

A Bluewaters XE node consists of 32 CPU cores with 32 GB of local memory. The unit of parallelism is a task, with one task requiring a single CPU core, and 20 placed per XE node. A task corresponds to the computation of a complete set of detection tests of fixed duration d and restricted to a 28-day sector, $|\mathbf{T}|_{d,N_q} \approx 10^7$. The detection tests are computed as described in Section 2.3.1. Each task is highly parallel, no communication is needed between

Table 2. Major Arithmetic Operations per Task

| Computation Type | Per task for transit Duration d |
|---|---|
| Single transit calculations (additions) | $\frac{N_q^2 \cdot d}{\delta e} \approx 10^{10}$ |
| Transit detection (multiplications and additions) | $(1 + \mu_t) \cdot N_q \cdot \mathbf{T} _{d, N_q} \approx 10^{11}$ |

NOTE—1) $\mathbf{T}|_{d, N_q}$ is the restriction of the transit search space \mathbf{T} to fixed duration d and length N_q ; of size $|\mathbf{T}|_{d, N_q}| \sim 10^7$ 2) A task is the computation of a complete set of transit detection tests of fixed duration for a single lightcurve in a 28-day TESS data segment. Numerical values computed for $d \sim 300$ LC samples. Note: $\log(N_q) > \mu_t \sim 3$.

Table 3. Memory Resources Per Task

| Resource Type | Resources per Task |
|----------------------------------|--------------------|
| Total Remote Disk Access (read) | 1.7 GB |
| Total Remote Disk Access (write) | 18 MB |
| Read Count | 2 |
| Write Count | 10^7 |
| Local Memory | 0.4 GB |

tasks. The approximate number and type of major arithmetic computations for a task are summarized in Table 2 for the transit search space in Table 1.

Since $\text{Cov}_{\mathbf{z}_i}^{-1} \sim 1.7$ GB, loading this full covariance for each task will hit a memory bottleneck when run in parallel. Hence we allocate tasks pertaining to the same lightcurve within a node, and load $\text{Cov}_{\mathbf{z}_i}^{-1}$ as a memory mapped object shared between the tasks. Within a task, single transit event statistics of the form $\text{Cov}_{\mathbf{z}_i}^{-1} \mathbf{t}_{d,s}$ are computed serially, only the $N_q \cdot D$ elements of the covariance matrix which are relevant to the single transit event $\mathbf{t}_{d,s}$ are read into local memory at a time.

The memory required to hold all single transit calculations per task is $\frac{N_q^2}{\delta e}$ float 32 values, of total size ~ 0.4 GB. All possible transit detection tests are output per sector, alongside the single transit detection tests.

The output of the detection tests is $|\mathbf{T}|_{d, N_q}| \approx 10^7$ float32 values, of total size 18 MB (therefore 10^7 writes per task). The individual detection results are intermediate as they are combined to form composite detection statistics as described below. Memory and I/O requirements (remote and local) per task are summarized in Table 3.

Each task corresponding to a sector must be complete (13 tasks per 1-year lightcurve) before they can be combined to compute detection tests corresponding to a year of data. The intermediate data output associated with a complete year, for all candidate durations, is of size $|\mathbf{T}|_{d, N_q} DQ|Y| \cdot 32 \sim 15$ TB. The detection tests are output for the full year for \mathbf{T} , requiring 1 GB per lightcurve.

2.4. Numerical Simulation

To evaluate the detector performance on TESS data for the specific pipeline implementation, we have conducted numerical single-transit injection tests using a subset of TESS light curves from year 1 and year 4. Additionally we compare performance to that of a standard pipeline analysis where detrending and detection are performed sequentially. Performance is evaluated via computing the detection efficiency, defined as the rate of correct recovery of an injected transit. This Section describes the setup of these numerical studies.

2.4.1. Injected Transit Signals

A total of 3000 single transit injection tests were performed, 1000 lightcurves were selected from 13 sectors of year 1 data, and a further 2000 lightcurves each from 2 sectors of year 4 (selected among sectors [40, 41, 42, 43]). Targets were randomly selected from available data. A synthetic transit is injected once per light curve, transit signals were simulated using the python transit¹² library developed by D. Foreman-Mackey. Synthetic transit signals include limb-darkening (Mandel & Agol 2002; Kipping 2013a) and a complete description of the transiting Keplerian orbital elements. The injected signals are drawn from a distribution of exoplanet population parameters given in Table 2.4.1. This population parameter distribution is informed by that used by Foreman-Mackey et al. (2015), Kipping (2013a), and Kipping (2013b).

Table 4. Injected Signal Parameter Distribution

| Transit Parameter | Distribution |
|---|----------------|
| Period P (days) | $U(1, 15.)$ |
| * | $U(1, 100.)$ |
| Radius ratio of planet to host star (%) | $U(0.01, 0.2)$ |
| Transit epoch t_0 (days) | $U(0, P)$ |
| Impact parameter (stellar radii) | $U(0, 1)$ |
| Argument of periape ω (rad) | $U(-\pi, \pi)$ |
| Limb darkening parameters: q_1, q_2 | $U(0, 1)$ |

NOTE—The distribution of injected signal parameters. A uniform probability density function over the domain $\{x_1, x_2\}$ is denoted as $U(x_1, x_2)$. (2000/3000) of the lightcurves selected from year 4 were injected with the period range (1,20), a further (1000/3000) of lightcurves selected from year 1 were generated with an extended period range (1,100). The limb-darkening parameters are defined in Kipping (2013a); see also Mandel & Agol (2002).

2.4.2. Injected Detection Tests

One objective of the detection tests is to understand the effect a transit signal has on the estimated noise priors. As such we estimate the noise models post transit injection, as per the procedure described in Section 2.1.5 and Section 2.1.4.

As in prior work, we adopt a standard detector for comparison to the joint detector described in Equation A2. In the standard model the cotrending is performed assuming the light curve contains no transit signal: $\mathbf{y}_i = \mathbf{s}_i + \mathbf{V}\mathbf{c}_i$, analogous to hypothesis H_0 (Equation 2). A maximum-a-posteriori (MAP), or equivalently minimum mean square error (MMSE), estimator for the systematic noise is constructed using the same Bayesian priors for systematic noise and stochastic noise as used in the detection model in Section 2.0.1.

$$\hat{\mathbf{c}}_{0,i}^{\text{MAP/MMSE}} = (\mathbf{V}^T \text{Cov}_{s,i}^{-1} \mathbf{V} + \text{Cov}_{c,i}^{-1})^{-1} (\mathbf{V}^T \text{Cov}_{s,i}^{-1} \mathbf{y}_i + \text{Cov}_{c,i}^{-1} \mu_{c,i}) \quad (12)$$

Detection is then performed on the cotrended light curves $\mathbf{y}_i^{\text{co}} = \mathbf{y}_i - \mathbf{V}\hat{\mathbf{c}}_{0,i}^{\text{MAP/MMSE}}$, which are modelled as containing stochastic noise \mathbf{s}_i . The standard detector is given by the following matched filter decomposed as in Section A:

$$T_i^{\text{co}}(\mathbf{y}_i^{\text{co}}) = \frac{1}{\sqrt{Q}} \sum_{q \in Q} \frac{\mathbf{y}_{i,q}^{\text{co},T} \text{Cov}_{\mathbf{s}_i(q)}^{-1} \mathbf{t}_q}{\sqrt{\mathbf{t}_q^T \text{Cov}_{\mathbf{s}_i(q)}^{-1} \mathbf{t}_q}} \underset{H_0}{\overset{H_1}{\gtrless}} \tau \quad (13)$$

For both the standard detector and our detector, a detection is considered to occur in a lightcurve \mathbf{y}_i if any of the candidate transit tests produces a test statistic $T(\mathbf{y}_i)$ above the threshold $\tau = 10$, we term the number of lightcurves with detections as N_d , and the total number of injected lightcurves as N . Among any detected transits, a correct detection occurs if the transit which produces the maximum test statistic matches the injected transit orbital period

¹² <http://dfm.io/transit>

to within 2 hours, the number of correct detections is termed N_c . The detection rate is calculated as the number of lightcurves with correct detection out of the number of injected lightcurves $\frac{N_c}{N}$. The quasi-false-alarm rate calculates the rate of incorrect detections among injected lightcurves $\frac{N_d - N_c}{N}$. A false-alarm (or incorrect detection) may in fact be a true transit with greater signal strength than an injected transit, therefore the detection rate estimates for weaker injected transits are subject to greater uncertainty. However it is generally expected that there is not a high density of transits in the sample lightcurves, and that they do not always exceed the detection strength of the injected transit such that the quasi-false-alarm rate reasonably identifies noise-properties or features that produce detection challenges. No post-processing was applied to the results of detection tests on injected lightcurves.

3. RESULTS

3.1. Injection Test Performance

We evaluate our detection performance with single-transit injection tests (Gilliland et al. 2000; Weldrake et al. 2005; Burke et al. 2006; Foreman-Mackey et al. 2015), the setup of these tests is described in Section 2.4. The maximum test statistic above threshold is used to quantify the detection rate, this is more restrictive than evaluating overall signal recovery as a transit signal may be among detections but fail to qualify as a correct detection if it does not produce the maximum statistic. Therefore the results of the injections tests are informative about sources of false alarm producing strong test statistics and inform false alarm rejection filtering described in Section 2.2. The results are shown separately for year 1 data (13 sectors in length) and the year 4 data (2 sectors in length), in order to study the effect of data length on signal recovery. In particular false alarms occurring either as repetitive sector-length systematic effects or outlier features occurring sparsely over a year of data. The detection efficiency of the standard detector, broken down by orbital period P and radius of planet-to-star ratio $\frac{R_p}{R_*}$ of the injected transit, is shown in Figure 13 for year 4 and Figure 15 for year 1. For our detector we display the difference in detection efficiency relative to the standard model, Figure 14 for year 4 in Figure 16 and for year 1.

Both our detector and the standard detector achieve a comparable rate of recovery for an achieved quasi-false alarm rate, with neither being clearly optimal. This result is consistent as a function of quasi-false-alarm rate plotted in Figure 18. This contrasts to achieved performance on Kepler data for which we demonstrated a clear detection improvement of $\sim 3\%$ of our detector over the standard detector, concentrated in short (< 3 day) period transits. We posit that TESS systematics as captured by the CBV's are subject to less uncertainty in TESS data and therefore more separable from transit events than those occurring in Kepler data. TESS was designed to minimize the impact of high magnitude systematics on observations, the strongest systematics that are present in TESS data have known physical origin due to momentum dumps and data downlinks and their signal form is well constrained as described in Section 2.1.4. Hence providing providing a greater degree of separability of transits and systematics by detrending in TESS data as compared to Kepler data, and Our detection method may not be directly beneficial here however may be well suited to sensors with a highly variable form of systematics. An example of the relative magnitude of the prior noise model is shown in Figure 12 whereby the standard deviation of each cadence under the joint prior is of the comparable magnitude to the contribution of the stellar prior alone.

Broadly the detectors show a high rate of signal recovery with a comparable false alarm rate, approximately achieving for the year-length tests 79% detection efficiency for 19% quasi-false-alarm rate. Over two sectors, the achieved detection efficiency is approximately 64% with a 6% quase-false-alarm rate. Since the noise characteristics and targets are distinct between year 1 and 4, there is expected variation in detection performance. In general the detection efficiency should be higher for year 1, as for a particular period/radius bin there are more transit events occurring in the data. By the same reasoning, an increase in false alarms is also expected, occurring due to the sector-to-sector periodic occurrence of residual systematics. For all data lengths we observe an expected drop off in detection efficiency for signals which produce a lower transit depth or for which there are fewer transit events.

The majority of false alarms are the result of residual systematics. In Figure 17 the density of detected periods for the sample of quasi-false-alarms is shown for both data samples, the majority of detected false alarms have a period between $10 - 15[days]$, and are the result of increased scatter at the edges of the $\sim 13.7[day]$ downlink cycle. In general we chose to the use the CBV's, due to the rigorous data analysis used to construct this basis. However the CBV's do not include edge flux ramps, as these are typically corrected via spline regression in an independent part of the SPOC pipeline. A future version of our pipeline would benefit from a basis set which is fully representative of the systematic effects present in a raw lightcurve. This effect is further investigated in the context of the TESS search results in

Section 3.2 where the same pattern of false alarms was observed. Additionally there is an increase in false-alarms increasing with orbital period due to outlier noise as described in Section 2.2.

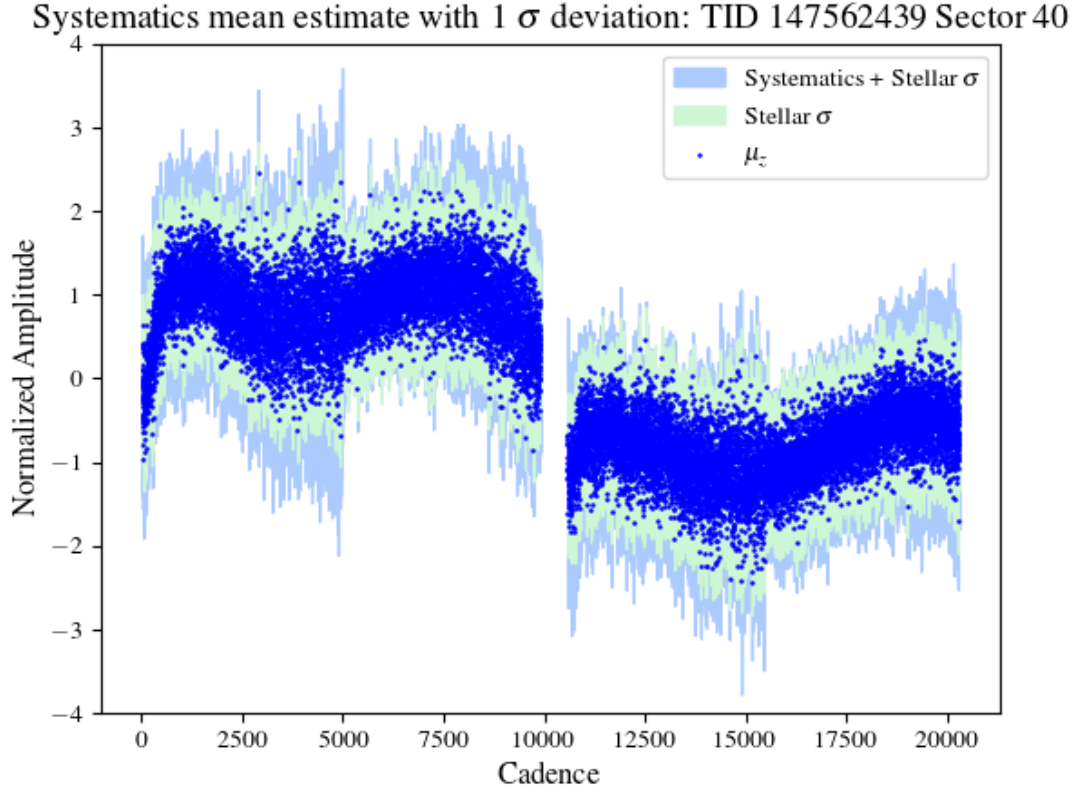


Figure 12. The mean of the joint noise model is plotted for a sample lightcurve in dark blue. Above and below each cadence the 1σ deviation of the stellar, and joint systematics and stellar prior for each cadence is shown. The relative uncertainty noise level of systematics and stellar noise is comparable.

<https://pyastronomy.readthedocs.io/en/latest/pyaslDoc/aslDoc/transitDuration.html> for calculation of duration

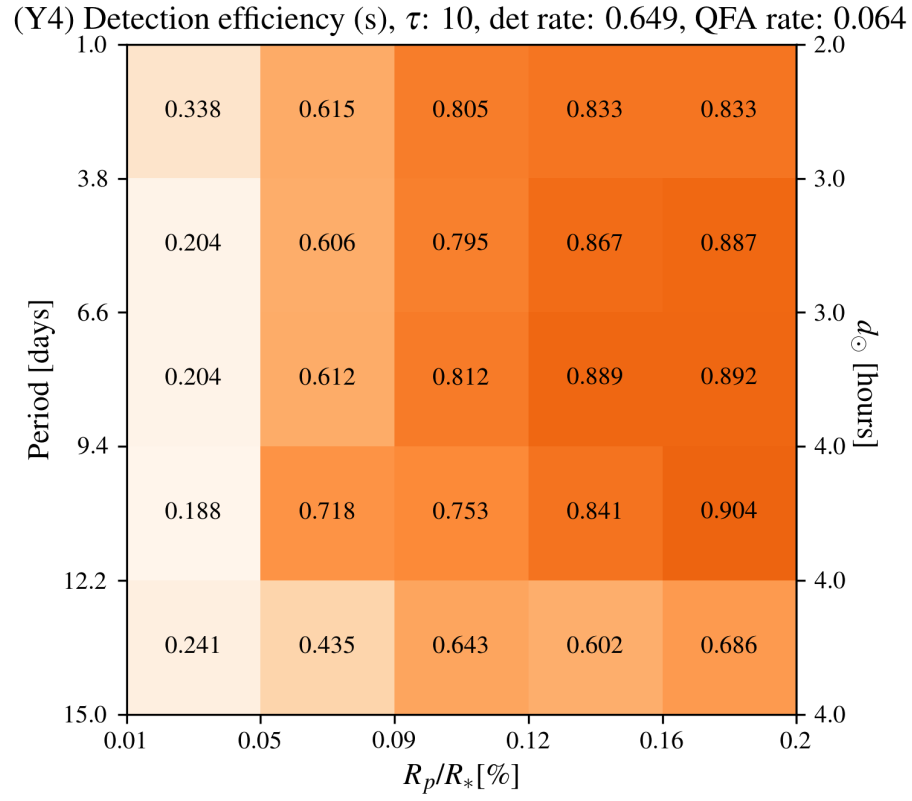


Figure 13. The standard model detection efficiency for a threshold of $\tau = 8.4$ computed using injection tests with lightcurves from year 4. The range of synthetic transit signal parameters can be found in Section 2.4.1.

(Y4) Detection efficiency difference (d - s), τ : 10, det rate: 0.004, QFA rate: -0.004

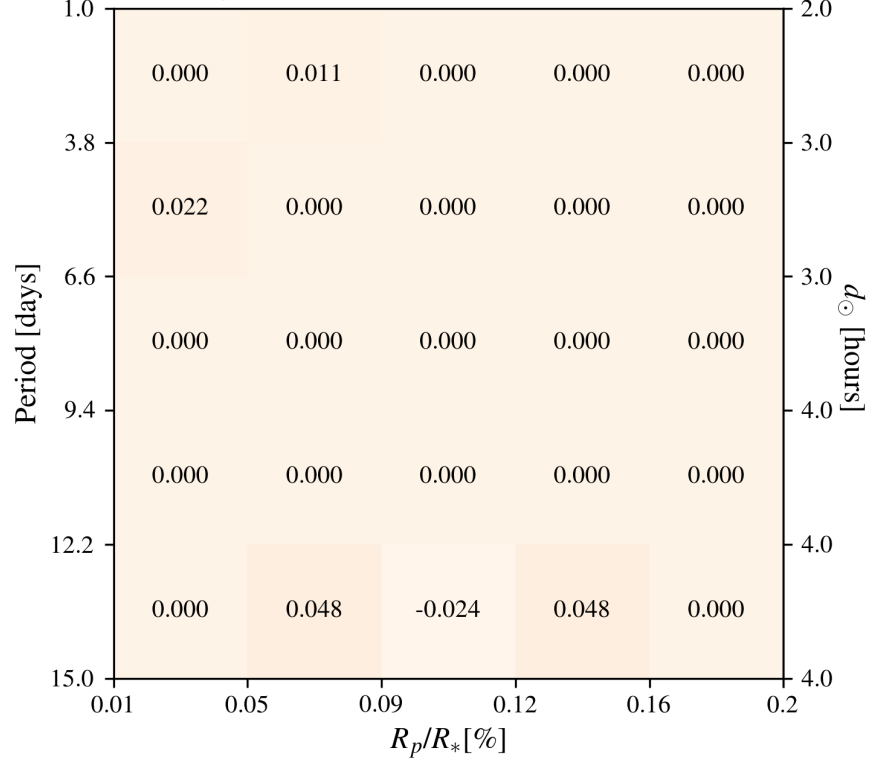


Figure 14. Detection efficiency compared to the standard detector for a threshold of $\tau = 8.4$ computed using injection tests with lightcurves from year 4. The range of synthetic transit signal parameters can be found in Section 2.4.1.

(Y1) Detection efficiency (s), τ : 10, det rate: 0.794, QFA rate: 0.195

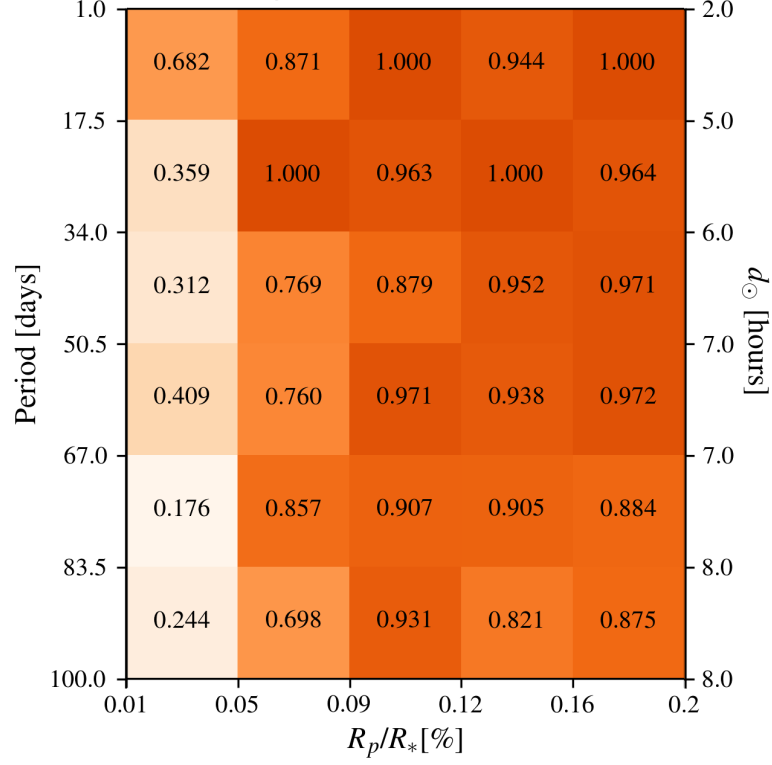


Figure 15. The standard model detection efficiency for a threshold of $\tau = 8.4$ computed using injection tests with lightcurves from year 1. The range of synthetic transit signal parameters can be found in Section 2.4.1.

(Y1) Detection efficiency difference (d - s), τ : 10, det rate: 0.0, QFA rate: 0.002

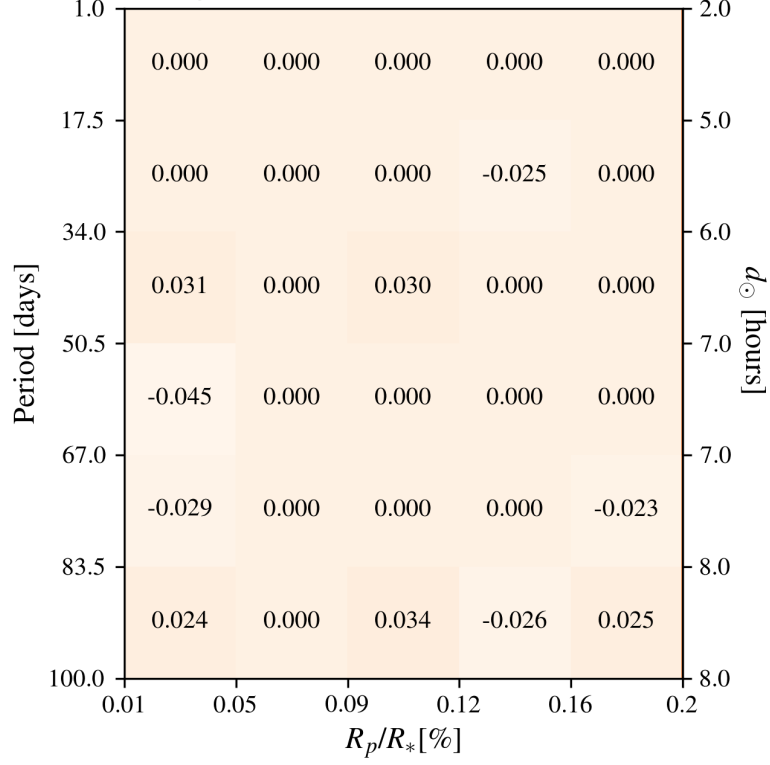


Figure 16. Detection efficiency compared to the standard detector for a threshold of $\tau = 8.4$ computed using injection tests with lightcurves from year 1. The range of synthetic transit signal parameters can be found in Section 2.4.1.

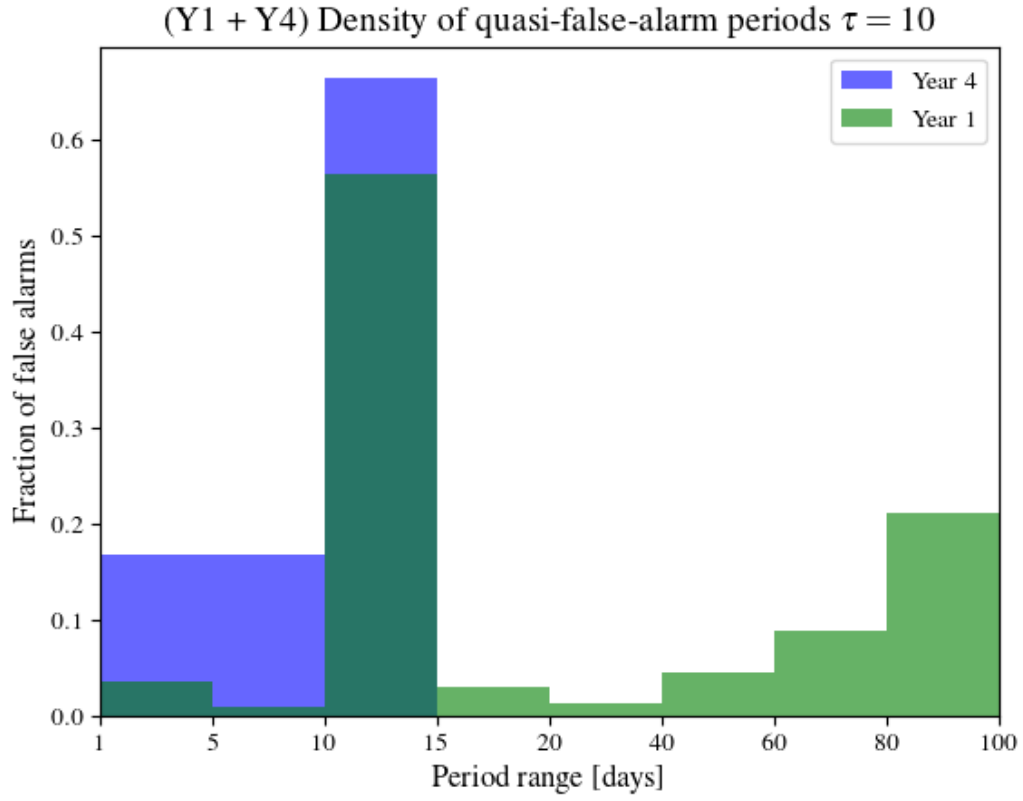


Figure 17. The density of the detected periods of injection test false alarms is shown. Either year is normalized to a density of 1, the false alarm rate for year 1 is 0.19, whereas for year 4 it is 0.06. In general it can be seen that over half of false alarms have a period between 10 – 15[days], this is likely due to systematics occurring on this timescale. Furthermore, there is a density of false alarms increasing with period.

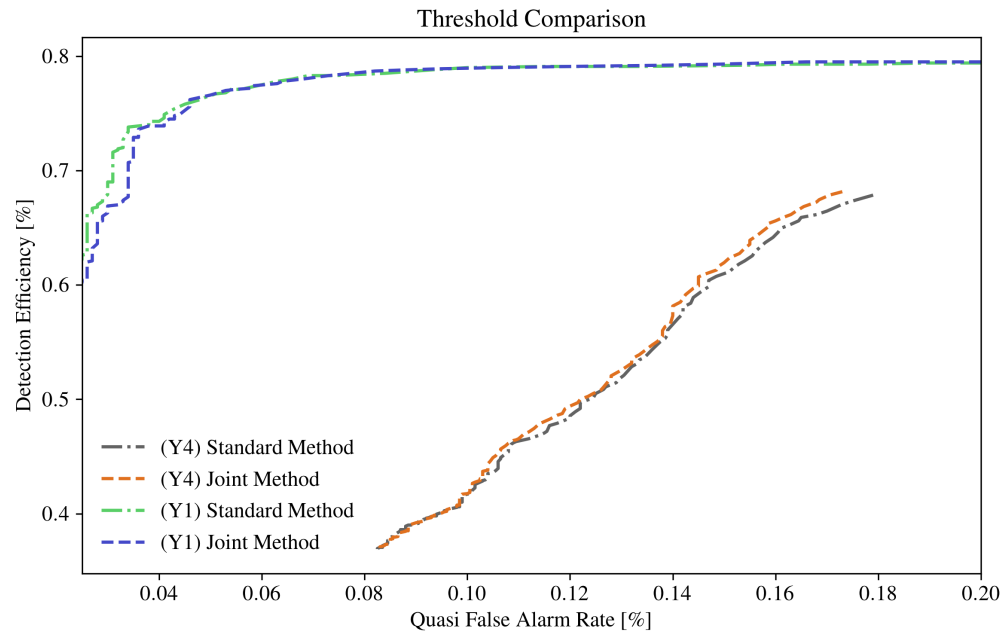


Figure 18.

3.2. TESS Search

As described in Section 2.1.2, the primary purpose of this work was to perform a search of the first 3 years of the TESS short cadence lightcurves from the CVZ. From this selection of lightcurves we did not remove TESS Objects of Interest (TOI) produced via the SPOC/QLP pipelines and used the selection of TOI present as a form of pipeline validation. We emphasize that we do not expect to, nor is it our intention, to recover the exact same TOI, however there is an expected overlap for transit signals of significant signal strength. Note that period range searched by the SPOC/QLP pipeline is different to ours, any candidate transits lying outside of our searched range are excluded from the listed TOI here.

Overall at a threshold of $\tau = 10$ and subject to heuristic filtering, described in Section 2.2.1 and Section 2.2.2, overall 28% of lightcurves contain a detection, with 551/1851 in year 1, 659/2046 in year 2 and 420/1922 in year 3. Among these detections, the criteria for a match, and the description of recovered TOI are described below in Section 3.2.1.

To produce a final list of candidates, we further use manual vetting. In particular even-odd phase folded lightcurves are used to identify eclipsing binaries, standard phase folded plots are also evaluated. The majority candidates between 10 – 15 days are excised as detected transits particularly contaminated by false alarms described in Section 3.1. Furthermore among lightcurves containing detections, 18 targets are listed as candidate eclipsing binaries in Prša et al. (2022), a further 81 targets are candidate eclipsing binaries in Prša et al. (2022) but we did not detect any transits among these targets. An example of a flagged eclipsing binary detected as an exoplanet transit is shown in Figure 24.

3.2.1. TOI Recovery

TOI are produced by filtering detections, termed threshold crossing events (TCE), from the QLP/SPOC pipeline. This includes both automated and manual vetting used to eliminate clear false alarms (i.e. systematics or statistical noise) or false positives (eclipsing binaries, sunspots) as described in (Guerrero et al. 2021). The TOI list used was downloaded from the ExoFOP database¹³, these are the product of both the SPOC/QLP searches. As noted on (<https://tess.mit.edu/toi-releases/>) there may be inconsistencies between the fitted parameters between the TOI lists produced by TSO, MAST and ExoFOP. Note that only a small fraction of TOI are confirmed planets.

For comparison of TOI recovery, we consider a candidate transit to be a match if for a target lightcurve i) there is a detection above a threshold of $\tau = 10$ and ii) the maximum candidate transit has an orbital period match to within 2hrs for any of the TOI candidate transits for the target under consideration. Theoretically any candidate transit consisting of true transit events, should produce a detection. A candidate transit with more transit events, should produce a larger detection statistic. However due to differing data masking, and or different noise or systematics models, what one detector may consider a true transit event, another may not. In a small number of cases, a detected period is an integer multiple (or vice versa) of a TOI candidate period. Therefore we also report a match if the detected period is (2, 3) integer multiple (or vice versa) of the TOI candidate period. Note that we only consider our top detection statistic above threshold, in most cases the TOI transit is among detections but is not be considered a match.

We report a high rate of TOI recovery of 65% over 3 years. In Table 5 the recovery is broken down by year, and the number of TOI present, the detection recall rate, the matched rate and the matched rate with false positive or false alarm TOI excluded. Considering the TOI present in the data, the rate of recovery is slightly increased for longer period TOI as shown in Figure 19 where the count is summarized over increasing period bins.

3.2.2. New Candidate Exoplanets

The search of TESS short cadence lightcurves from the CVZ produced detections in approximately 28% of lightcurves at a detection threshold of $\tau = 10$. The detection threshold was set based on the injection tests and to reasonably suppress the number of targets containing detections while maintaining sensitivity to weak transit signals. Heuristic thresholding of detected transits using the variance metric described in Section 2.2.1 was used to remove outliers in long-period detections, alongside thresholding of candidate detections with a correlation metric described in Section 2.2.2 close to zero. The metrics are somewhat robust to outlier signals, however are not robust to noise producing transit-like signals.

The distribution of detected periods is shown in Figure 21 where there is a density of detections between 10–20[days]. This distribution of detected periods mirrors the distribution of quasi-false alarm periods for the injection tests 3.1.

¹³ <https://exofop.ipac.caltech.edu/tess/>

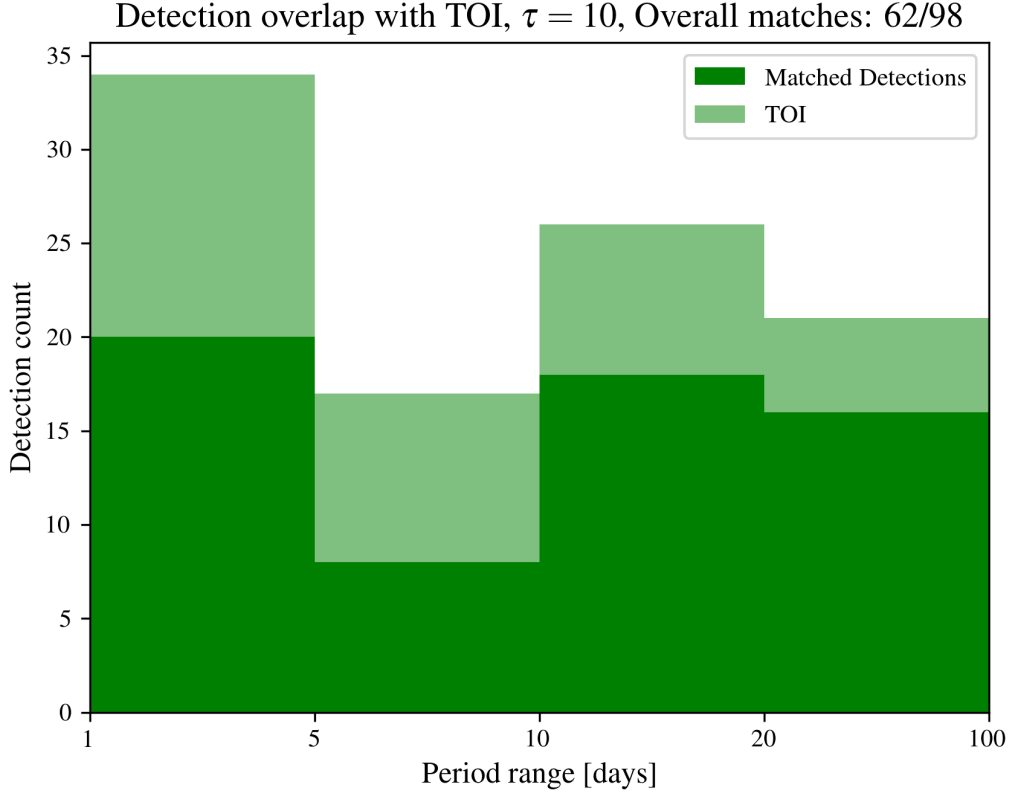


Figure 19. The pipeline detections for which the leading detected transit is matched to a TOI are shown overlaid and broken down by period range.

Table 5. TOI matched detections $\tau = 10$

| | TOI in target selection | TOI detections | Recall rate | TOI match | Match rate | Match rate (FP/FA filtered) |
|---------|-------------------------|----------------|-------------|-----------|------------|-----------------------------|
| Year 1 | 30 | 23 | 76 % | 17 | 57 % | 55 % |
| Year 2 | 21 | 18 | 86 % | 15 | 71 % | 68 % |
| Year 3 | 47 | 34 | 72 % | 30 | 64 % | 64 % |
| Overall | 98 | 75 | 77 % | 62 | 63 % | 62 % |

NOTE—TOI matched detection for a detection threshold of $\tau = 10$. The first column is the number of lightcurves with TOI present, the second column is the number of TOI which are among all detections above threshold, in the third column the recall rate is given (TOI detections / TOI in target selection). A TOI match is considered to occur if the transit above threshold with maximum detection statistic has an orbital period which matches the TOI, see Section 3.2.1 for a full description of this criteria. The fourth column is the number of TOI matches, with this rate provided in the fifth column (TOI match / TOI in target selection). The sixth column is the match rate with any TOI which are designated as false positives (FP) or false alarms (FA) excluded.

Generally this suggests a large number of these detections are false-alarms. In figure 20 the density of distributions with an orbital period between 1 – 19 days is plotted against the associated detection statistic. In Figure 22 detected transits between 11 – 15 days are shown to be correlated with times of large scatter due to data downlinks, suggesting a density of false alarms in this period range. Furthermore there are a number of short period false alarms, expected due to quasi-periodic stellar variability as observed in Kepler TCE's (Thompson et al. 2018). A final set of 50 new candidate exoplanets are produced in Table 7 by manual vetting of the detections.

Table 6. New Exoplanet Candidates and Properties

| TID | R.A. (J2000) | Decl. (J2000) | TESS mag | Period [days] | Dur [hours] | Epoch [BJD-2457000] |
|-----------------|--------------|---------------|----------|---------------|-------------|---------------------|
| 382 391947345 | 107.944043 | -74.610270 | 11.76 | 11.48 | 14 | 1332.27 |
| 241 229487733* | 296.140262 | 62.612247 | 10.65 | 13.33 | 10 | 1693.76 |
| 1642 1551345499 | 277.292595 | 55.313667 | 10.30 | 47.41 | 4 | 1701.38 |
| 14 277021897 | 83.923330 | -69.854133 | 10.52 | 8.14 | 16 | 2039.97 |
| 91 348842168 | 98.855681 | -57.271547 | 11.49 | 13.92 | 6 | 2045.44 |
| 113 179576115 | 80.445744 | -71.328863 | 9.99 | 5.06 | 6 | 2037.27 |
| 143 389323171 | 85.665373 | -70.731037 | 12.25 | 1.62 | 10 | 2036.12 |
| 211 382435735 | 117.249265 | -65.588492 | 10.77 | 6.99 | 3 | 2042.54 |
| 372 30275829 | 74.003721 | -66.437942 | 11.70 | 8.11 | 12 | 2038.07 |
| 430 141866704 | 93.859849 | -75.253218 | 10.41 | 1.42 | 4 | 2037.28 |
| 593 30275861 | 74.180044 | -66.417382 | 12.17 | 1.10 | 4 | 2036.73 |
| 670 141811446 | 92.671726 | -77.469917 | 12.82 | 3.57 | 8 | 2037.12 |
| 762 391925531 | 107.735210 | -76.112138 | 10.64 | 43.95 | 6 | 2078.97 |
| 1480 140900726 | 77.119547 | -75.483607 | 13.24 | 4.65 | 10 | 2039.35 |
| 1492 300013489 | 107.009117 | -67.663764 | 13.28 | 5.22 | 4 | 2040.63 |
| 1639 364538560 | 71.077316 | -74.205836 | 11.32 | 1.75 | 4 | 2037.62 |
| 1788 141770592* | 92.099821 | -77.653516 | 9.77 | 12.13 | 6 | 2048.11 |
| 1833 350274840 | 83.367769 | -58.737608 | 11.68 | 1.60 | 3 | 2037.09 |

NOTE—Candidates marked with an asterisk are also marked as CTOI by other users.

Table 7. New Candidate Eclipsing Binaries

| TID | R.A. (J2000) | Decl. (J2000) | TESS mag | Period [days] | Dur [hours] | Epoch [BJD-2457000] |
|-----------|--------------|---------------|----------|---------------|-------------|---------------------|
| 30275861 | 74.180044 | -66.417382 | 12.17 | 1.10 | 10 | 2036.73 |
| 140802498 | 75.126779 | -73.089399 | 10.88 | 3.97 | 3 | 2038.24 |
| 55650494 | 73.846709 | -62.750057 | 12.41 | 5.61 | 3 | 2038.31 |
| 278825952 | 100.470628 | -55.794997 | 11.46 | 2.39 | 4 | 2036.65 |

NOTE—A list of new eclipsing binaries which are not already listed under the eclipsing binary catalog. See [Prša et al. \(2022\)](#). For a full candidate list.

4. DISCUSSION

The pipeline performance over single-transit injection tests in Section 3.1 showed comparable performance when comparing the joint detector to a standard detector defined in Section 2.4. It is important to note that our standard detector, which performs detrending and detection as two separate and sequential steps, is implemented as a modification of our pipeline. As described, there are a number of major differences between our pipeline and other pipelines using a standard detection model and we do not claim to use our comparative injection tests to reflect the performance of these alternate pipelines. Our detector achieves a detection rate of 79% at a 19% quasi-false-alarm rate for single-transit injection tests performed over a year of data, approximately the same rate is achieved by the standard approach. We posit similar performance between the methods is due to the nature of TESS systematics as captured by the CBV's, which are generally well constrained and separable from transit signals as compared to Kepler systematics. However, the joint method may be beneficial applied to sensors where there is a high level of uncertainty of systematics, as this method allows inherent uncertainty to be marginalized over with respect to a continuous range of noise models.

Key challenges still exist in searching TESS data. The results of this work are highly dependent on a number of implementation choices, such as search space discretization and chosen noise priors. Additionally residual systematics,

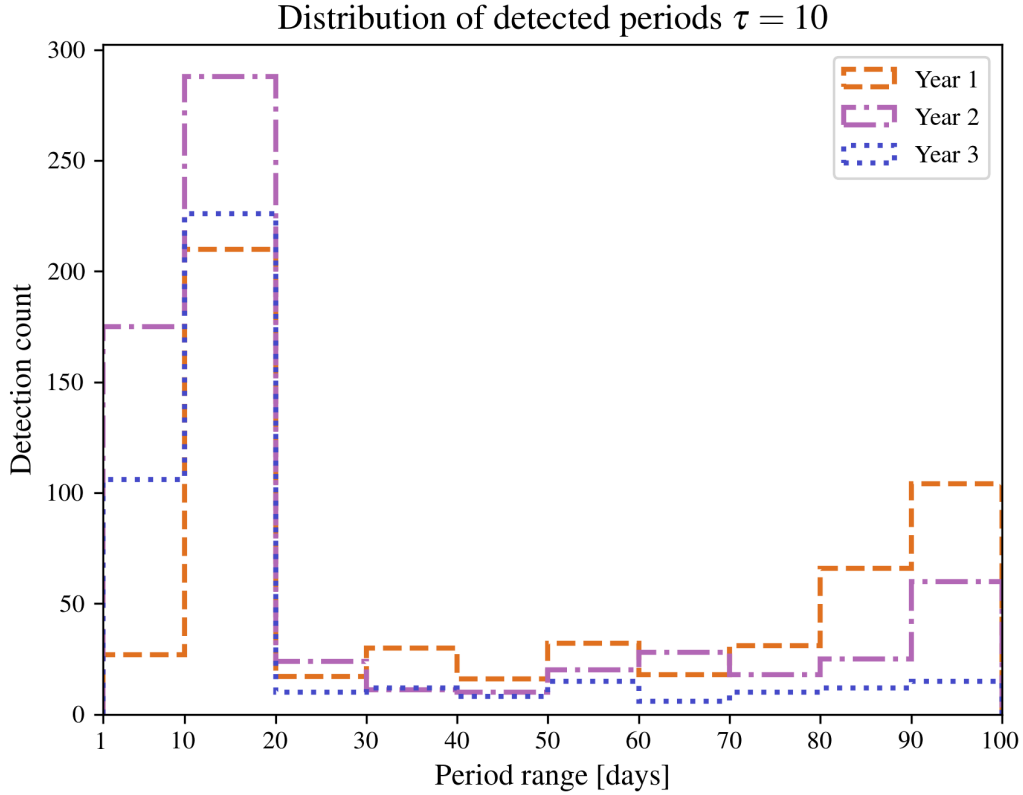


Figure 20. The pipeline detections broken down by period range.

unmodeled by the CBVs, cause an excess of false alarm detections at short periods due to excess scatter prior to momentum dumps occurring periodically between 2 – 5 days and around the 13.7 day downlink cycle. The choice to use CBVs is motivated by the high level of analysis used to construct them. However, in the SPOC pipeline CBVs are used alongside polynomial detrending to remove systematics. We suggest a future version of our pipeline would benefit from a complete systematics basis set.

In this work we addressed the computational challenges associated with the joint method, described in the METHODS section, in order to search 3 years of TESS short cadence data for transits with periods between 1 – 100 days. The developed pipeline is robust to spurious harmonics occurring due to stellar variability alongside systematics, in particular gap-filling or stitching is not a theoretical requirement of our pipeline. Furthermore we provide theoretically motivated filtering methods to remove false alarms occurring as long period transit signals. These post-processing metrics require further investigation to fully validate their performance, which we leave to future work.

The lightcurves searched contain a small sample of TOI, our recovery of these TOI is compared using a match criterion described in Section 3.2.1. Subject to the post-processing described in Section 2.2, approximately 77% of TOI are recovered with our pipeline, with higher recovery in TOI with periods > 10 days. Of the TOI present, 65% are recovered as the detection above threshold with maximum statistic. We note that different pipelines may produce different candidates, the intention of this work is to obtain new candidates.

Overall approximately 28% of target lightcurves contain detections, a large number of which are determined to be spurious detections due to unmodeled systematics or outlier noise. In Figure 20] the overall density of detections is shown for the period range between 1-100 days. Over half of the detected transits have an orbital period between 1 – 20 days. In Figure 21 a histogram of detected periods and their associated transit detection statistics are shown, we note that the results shown are from post-processed detections whereby a number of weak signals have been removed. Primarily the detections between 1 – 19 days consist of weak statistics, and are concentrated between 1 – 3 days and 11 – 15 days. This pattern reflects the observed density of SPOC TCE’s as a function of period (Fausnaugh et al.

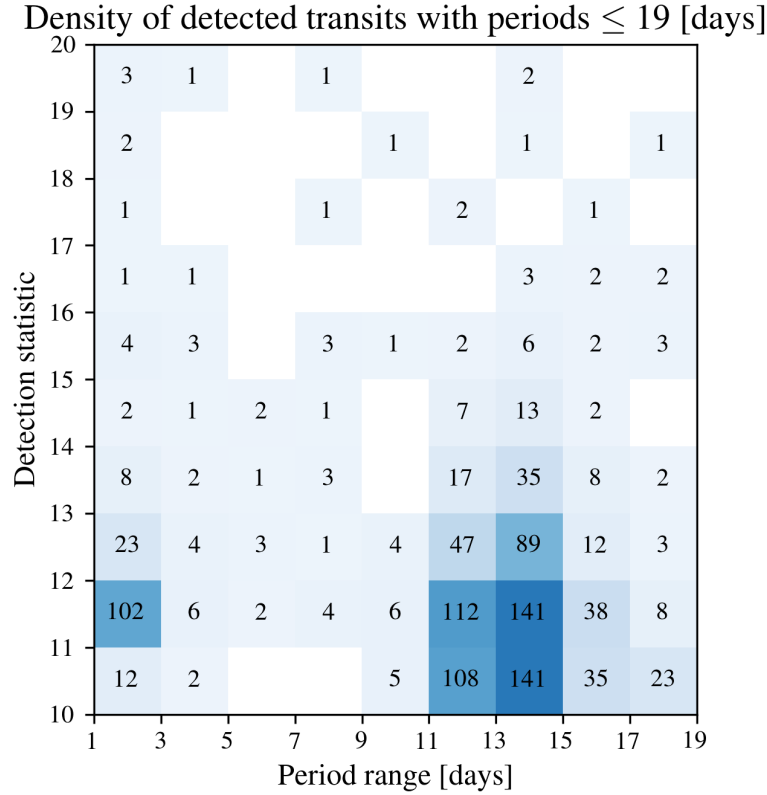


Figure 21. Histogram of detected periods (≤ 19 [days] and detection test statistic $T(\mathbf{y}) \leq 20$) all three years combined.

2018) (p 17.). The density in false alarms occurring between 11 – 15 days is determined to be the result of residual systematics occurring due to the TESS downlink cycle. An excess of detections for short-period transits was observed for Kepler (Thompson et al. 2018) and TESS TCE’s (Fausnaugh et al. 2018) (p 17.) attributed to quasi-sinusoidal variable stars and residual systematics due to the momentum dump cycle. Unmodeled systematics may be partially corrected by the skyline filtered correlation metric.

As discussed in Section 2.2 the stochastic noise model may not always be accurate and may fail to reflect local variations. Times of excess scatter occurring over a sector contribute to spurious long-period transit detections. This is reflected in an excess of detections occurring at long-periods in Figure 20. The form of stochastic noise prior may be improved as non-stationary, and using a local estimator.

A list of new candidate exoplanets is produced in Table 7. These candidates are produced by manual vetting of detections, to eliminate eclipsing binaries, stellar harmonics or transit-like noise. These candidates are listed as Community Tess-Objects-of-Interest (CTOI) in the ExoFOP database¹⁴ with median binned and phase folded lightcurves, and even-odd phase folded figures.

5. CONCLUSIONS

In this work we applied a joint detection method with Bayesian priors for systematic and stochastic noise to search for exoplanet transits in three years of TESS short cadence lightcurves from the continuous viewing zone. We develop a pipeline to address unique aspects of TESS data, including pre-processing (masking of data and estimation of priors), and post-processing (filtering of false alarms). We address computational challenges of the joint detection method, and described an efficient implementation based on a sector-wise decomposition of the joint detector, and utilizing overlap in the space of searchable candidate transit signals. Furthermore our resulting pipeline performance is evaluated in

¹⁴ exofop.ipac.caltech.edu/tess/view_ctoi.php

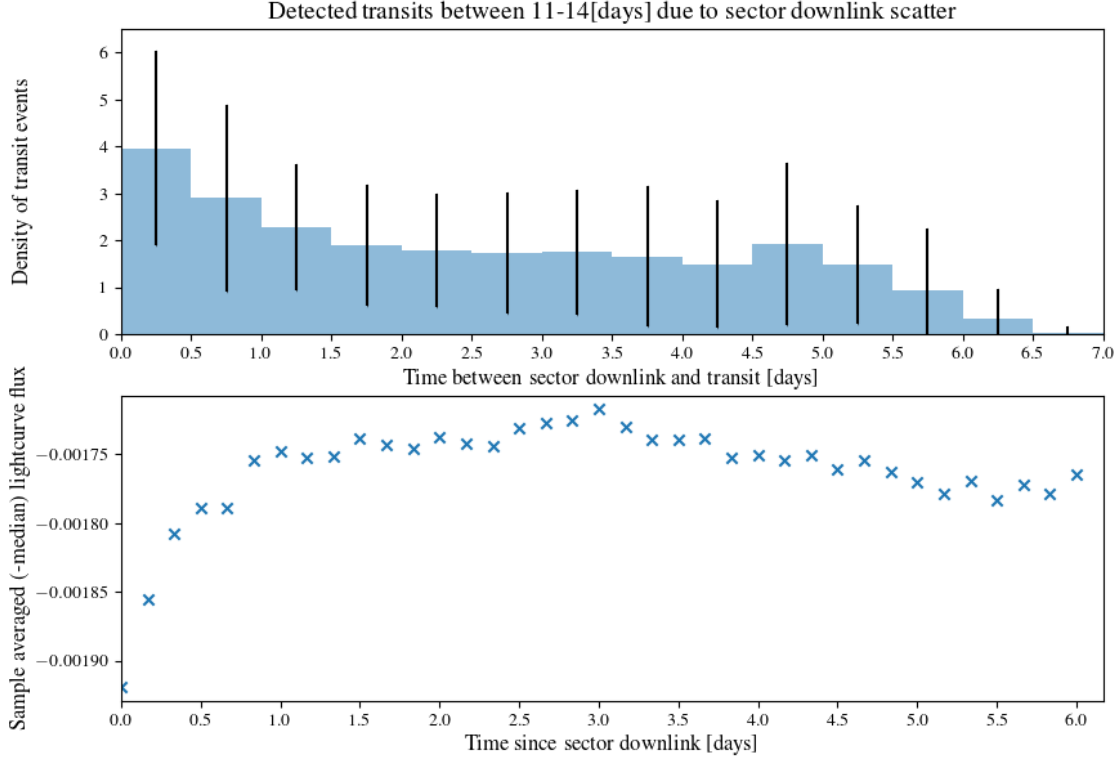


Figure 22. Top figure 1/2 day bin size, average density of transit events per lightcurve, error bar refers to standard deviation of this density between lightcurves. Bottom figure 4 hour bin size, mean of negative flux. Increased negative scatter at sector edges, and correlated with location of detected transit events, suggesting a large density of detections between 11-14 days are false alarms induced by negative scatter due to sector downlink.

numerical recovery tests of injected transit signals added to raw TESS light curves. These tests examine the joint method and a modified version of our pipeline designed to perform detrending as a prior step to detection, termed the standard method.

- The results of our injection tests show a high level of detection efficiency 79% with a 19% quasi-false-alarm rate, however no clear benefit is shown as compared a standard method. We attribute this result to the nature of TESS systematics, but propose the joint method may be beneficial for detection on a sensor where systematics noise levels are high and variable in form. Our pipeline may also benefit from a complete set of systematics basis vectors to replace the use of cotrending basis vectors which were not designed to be standalone.
- In our full-scale search of three years of TESS short cadence lightcurves from the CVZ approximately 28% of lightcurves have a detection above threshold. Among the top detected transit for these lightcurves we recover 65% of TOI with matching orbital period and achieve a 77% recall rate for TOI among all our detected transits.
- Due to residual systematics unmodelled by the CBVs (and corrected by ancillary processing in the SPOC pipeline), we have a large number of false alarms between 10 – 15 days. From further manual vetting of the detections we produce 16 new candidate exoplanets.

6. ACKNOWLEDGEMENTS

This research is part of the Blue Waters sustained-petascale computing project, which is supported by the National Science Foundation (awards OCI-0725070 and ACI-1238993) and the state of Illinois. Blue Waters is a joint effort of the University of Illinois at Urbana-Champaign and its National Center for Supercomputing Applications.

This paper includes data collected with the TESS mission, obtained from the MAST data archive at the Space Telescope Science Institute (STScI). Funding for the TESS mission is provided by the NASA Explorer Program.

Even Odd Phase Folded Lightcurve TID: 55650494, stat: 1450

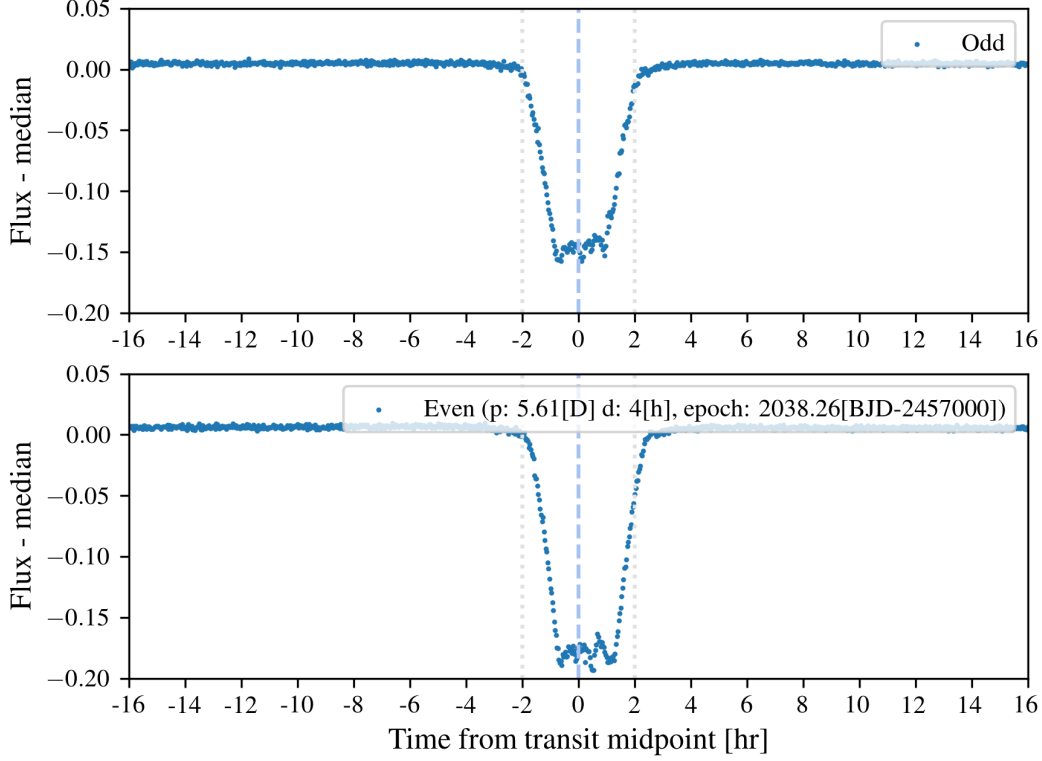


Figure 23. Even and odd phase folded lightcurves are shown for a candidate eclipsing binary from year 3. The fitted parameters (period p , duration d and epoch) are shown in the key. Uneven transit depths indicate this detected transit is likely an eclipsing binary star

STScI is operated by the Association of Universities for Research in Astronomy, Inc., under NASA contract NAS 5-26555.

This research has made use of the Exoplanet Follow-up Observation Program (ExoFOP; DOI: 10.26134/ExoFOP5) website, which is operated by the California Institute of Technology, under contract with the National Aeronautics and Space Administration under the Exoplanet Exploration Program.

APPENDIX

A. SECTOR-TO-SECTOR DETECTOR

A year long TESS lightcurve consists of 13 sectors of data. In our pipeline noise is modelled as independent between sectors. The noise \mathbf{z}_i is described by a covariance of the form $\text{Cov}_{\mathbf{z}_i} = \text{Cov}_{\mathbf{s}_i} + \mathbf{V}\text{Cov}_{\mathbf{c}}\mathbf{V}^T$. Systematics are estimated sector to sector, therefore the term $\mathbf{V}\text{Cov}_{\mathbf{c}}\mathbf{V}^T$ admits a block diagonal structure, where each block is the covariance model $\mathbf{V}_q\text{Cov}_{\mathbf{c}(q)}\mathbf{V}_q^T$ for a single sector $q \in Q$. A similar block diagonal structure is adopted for the stochastic noise, since a sector long model reasonably accounts for variability occurring on transit timescales. For a sector q the noise covariance is of the form $\text{Cov}_{\mathbf{z}_i(q)} = \text{Cov}_{\mathbf{s}_i(q)} + \mathbf{V}\text{Cov}_{\mathbf{c}(q)}\mathbf{V}^T$. The structure of the noise covariance for all sectors is given as:

$$\text{Cov}_{\mathbf{z}_i} = \begin{bmatrix} \text{Cov}_{\mathbf{z}_i(1)} & & & \\ & \text{Cov}_{\mathbf{z}_i(2)} & & \\ & & \ddots & \\ & & & \text{Cov}_{\mathbf{z}_i(Q)} \end{bmatrix} \quad (\text{A1})$$

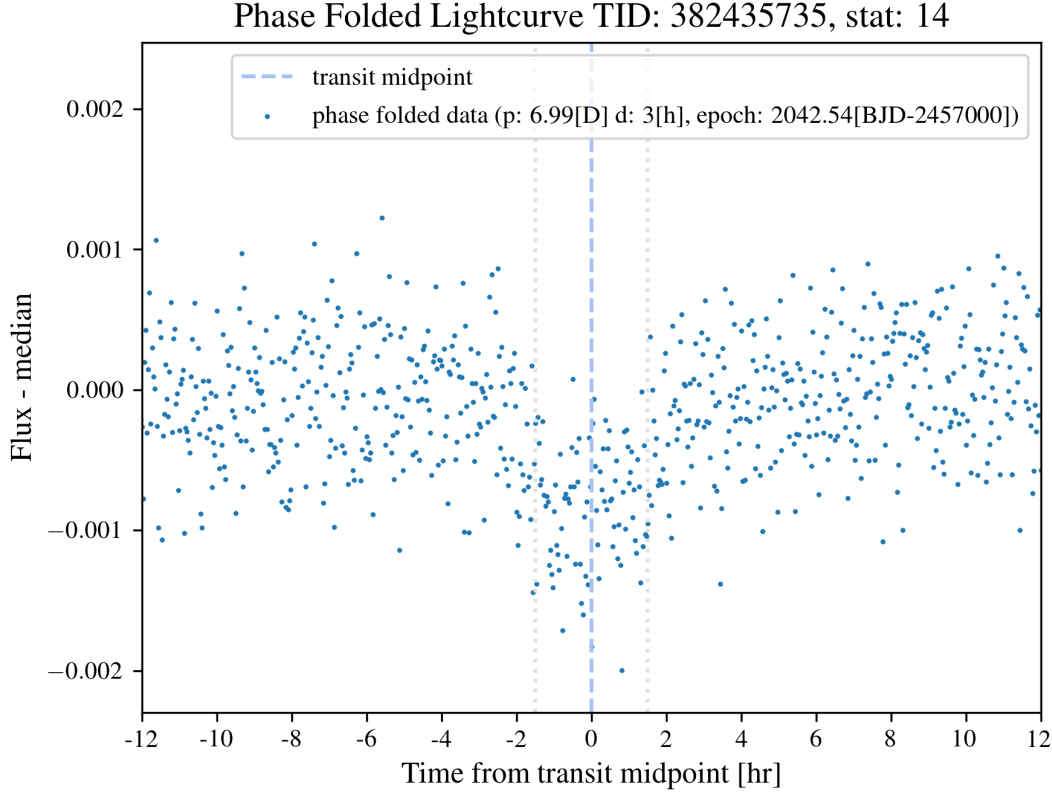


Figure 24. A phase-folded lightcurve is shown for a new exoplanet candidate. The estimated radius of $2.3R_{\odot}$ ($R_p/R_s : 0.0196$).

Due to the properties of block-diagonal matrices, the inverse covariance $\text{Cov}_{\mathbf{z}_i}^{-1}$ also admits a block-diagonal structure and each block $\text{Cov}_{\mathbf{z}_i}^{-1}|_q$ can be computed as the inverse of the corresponding sector $\text{Cov}_{\mathbf{z}_i(q)}^{-1}$. The block diagonal structure of $\text{Cov}_{\mathbf{z}_i}^{-1}$ allows the matched filter described in Equation 5 to be decomposed across multiple sectors $q \in Q$ as:

$$\frac{\sum_{q \in Q} \hat{\mathbf{y}}_{i,q}^T \text{Cov}_{\mathbf{z}_i(q)}^{-1} \mathbf{t}_q}{\sqrt{\sum_{q \in Q} \mathbf{t}_q^T \text{Cov}_{\mathbf{z}_i(q)}^{-1} \mathbf{t}_q}} \underset{H_0}{\overset{H_1}{\gtrless}} \tau \quad (\text{A2})$$

The matched filter is a normalized detector, scaling the candidate transit signal by $\alpha \in \mathbb{R}^+$ will not effect the detection statistic. Therefore a candidate transit depth is not needed to parameterize \mathbf{T} .

However to correctly compute Equation A2, the lightcurve broken up by sector $\hat{\mathbf{y}}_{i,q}$ must be normalized so that the transit strength is constant for all sectors. In our implementation, we chose to compute detection statistics restricted per sector, and form an approximation of Equation A2 with the normalized sum of these matched filters. Practically this means there is no need to normalize the lightcurve $\hat{\mathbf{y}}_{i,q}$ and reduced the intermediary data output.

$$T(\mathbf{y}_i) = \frac{1}{\sqrt{Q}} \sum_{q \in Q} \frac{\hat{\mathbf{y}}_{i,q}^T \text{Cov}_{\mathbf{z}_i(q)}^{-1} \mathbf{t}_q}{\sqrt{\mathbf{t}_q^T \text{Cov}_{\mathbf{z}_i(q)}^{-1} \mathbf{t}_q}} \underset{H_0}{\overset{H_1}{\gtrless}} \tau \quad (\text{A3})$$

B. AVERAGE NUMBER OF TRANSIT EVENTS μ_T IN CANDIDATE SEARCH SPACE \mathbf{T} IS CONSTANT FACTOR

Consider a lightcurve of length N , and a candidate transit space step-size δ_e in orbital period P and epoch t_0 . For ease of calculation consider the number of 'samples' as $\frac{N}{\delta_e}$, and $P \in \{1, \frac{N}{2\delta_e}\}$, with $t_0 \in \{1, P\}$ with a step-size of 1. The number of transit events occurring in a candidate transit signal with period P is approximately $\frac{N}{\delta_e P}$, and ranges

between $\{2, \frac{N}{\delta_e}\}$. Therefore the average number of transit events over \mathbf{T} is constant factor, where non-asymptotic terms are dropped:

$$\mu_t = \frac{1}{\sum_{i=2}^{\frac{N}{\delta_e}} i} \cdot \sum_{i=2}^{\frac{N}{\delta_e}} i \frac{N}{\delta_e i} \sim 2 \quad (\text{B4})$$

REFERENCES

- Aigrain, S., Parviainen, H., & Pope, B. J. S. 2016, *Monthly Notices of the Royal Astronomical Society*, 459, 2408. <https://doi.org/10.1093/mnras/stw706>
- Angus, R., Morton, T., Aigrain, S., Foreman-Mackey, D., & Rajpaul, V. 2017, *Monthly Notices of the Royal Astronomical Society*, 474, 2094. <https://doi.org/10.1093/mnras/stx2109>
- Auvergne, M., Bodin, P., Boissard, L., et al. 2009, *Astronomy & Astrophysics*, 506, 411
- Borucki, W. J., Koch, D., Basri, G., et al. 2010, *Science*, 327, 977
- Burke, C. J., Gaudi, B. S., DePoy, D., & Pogge, R. W. 2006, *The Astronomical Journal*, 132, 210
- Chakraborty, J., Wheeler, A., & Kipping, D. 2020, *Monthly Notices of the Royal Astronomical Society*, 499, 4011
- Christiansen, J. L., Clarke, B. D., Burke, C. J., et al. 2013, *The Astrophysical Journal Supplement Series*, 207, 35. <https://doi.org/10.1088%2F0067-0049%2F207%2F2%2F35>
- Cunningham, J. P., & Ghahramani, Z. 2015, *J. Mach. Learn. Res.*, 16, 2859–2900. <https://dl.acm.org/doi/10.5555/2789272.2912091>
- Deeg, H. J., & Alonso, R. 2018, *Transit Photometry as an Exoplanet Discovery Method* (Cham: Springer International Publishing), 1–25. https://doi.org/10.1007/978-3-319-30648-3_117-1
- Eisner, N. L., Barragán, O., Lintott, C., et al. 2020, *Monthly Notices of the Royal Astronomical Society*, 501, 4669. <https://doi.org/10.1093/mnras/staa3739>
- Fausnaugh, M. M., Caldwell, D. A., Jenkins, J. M., et al. 2018, *TESS Data Release Notes: Sector 1, DR1*, Tech. rep.
- Foreman-Mackey, D., Montet, B. T., Hogg, D. W., et al. 2015, *The Astrophysical Journal*, 806, 215
- Gilliland, R. L., Brown, T. M., Guhathakurta, P., et al. 2000, *ApJL*, 545, L47
- Guerrero, N. M., Seager, S., Huang, C. X., et al. 2021, *ApJS*, 254, 39
- Hedges, C., Angus, R., Barentsen, G., et al. 2020, *Research Notes of the American Astronomical Society*, 4, 220
- Huang, C. X., Vanderburg, A., Pál, A., et al. 2020, *Research Notes of the AAS*, 4, 204. <https://doi.org/10.3847/2515-5172/abca2e>
- Jara-Maldonado, M., Alarcon-Aquino, V., Rosas-Romero, R., Starostenko, O., & Ramirez-Cortes, J. M. 2020, *Earth Science Informatics*, 13, 573
- Jenkins, J. M., Chandrasekaran, H., McCauliff, S. D., et al. 2010, in *Software and Cyberinfrastructure for Astronomy*, ed. N. M. Radziwill & A. Bridger, Vol. 7740, International Society for Optics and Photonics (SPIE), 140 – 150. <https://doi.org/10.1117/12.856764>
- Jenkins, J. M., Twicken, J. D., McCauliff, S., et al. 2016, in *Society of Photo-Optical Instrumentation Engineers (SPIE) Conference Series*, Vol. 9913, *Software and Cyberinfrastructure for Astronomy IV*, ed. G. Chiozzi & J. C. Guzman, 99133E
- Kay, S. M. 1993, *Fundamentals of statistical signal processing*, Prentice Hall signal processing series (Upper Saddle River, NJ: Prentice Hall PTR). <http://cds.cern.ch/record/2012069>
- Kipping, D. M. 2013a, *Monthly Notices of the Royal Astronomical Society*, 435, 2152. <https://doi.org/10.1093/mnras/stt1435>
- . 2013b, *Monthly Notices of the Royal Astronomical Society: Letters*, 434, L51. <https://doi.org/10.1093/mnrasl/slt075>
- Lund, M. N., Handberg, R., Buzasi, D. L., et al. 2021, *The Astrophysical Journal Supplement Series*, 257, 53
- Mandel, K., & Agol, E. 2002, *The Astrophysical Journal Letters*, 580, L171
- Mendes, C. L., Bode, B., Bauer, G. H., et al. 2015, *Journal of Computational Science*, 10, 327. <https://www.sciencedirect.com/science/article/pii/S1877750315000344>
- Nguyen, T., Morgan, E., Vanderspek, R., et al. 2018, *Journal of Astronomical Telescopes, Instruments, and Systems*, 4, 1. <https://doi.org/10.1117/1.JATIS.4.4.047001>
- Prša, A., Kochoska, A., Conroy, K. E., et al. 2022, *The Astrophysical Journal Supplement Series*, 258, 16. <https://doi.org/10.3847/1538-4365/ac324a>

- Rasmussen, C. E. 2003, in *Summer school on machine learning*, Springer, 63–71
- Ricker, G. R., Winn, J. N., Vanderspek, R., et al. 2014, *Journal of Astronomical Telescopes, Instruments, and Systems*, 1, 1 .
<https://doi.org/10.1117/1.JATIS.1.1.014003>
- Roberts, S., McQuillan, A., Reece, S., & Aigrain, S. 2013, *Monthly Notices of the Royal Astronomical Society*, 435, 3639. <https://doi.org/10.1093/mnras/stt1555>
- Santerne, A., Fressin, F., Díaz, R. F., et al. 2013, *A&A*, 557, A139
- Seader, S., Tenenbaum, P., Jenkins, J. M., & Burke, C. J. 2013, *The Astrophysical Journal Supplement Series*, 206, 25. <https://doi.org/10.1088/0067-0049/206/2/25>
- Smith, J. C., Stumpe, M. C., Cleve, J. E. V., et al. 2012, *Publications of the Astronomical Society of the Pacific*, 124, 1000.
<http://stacks.iop.org/1538-3873/124/i=919/a=1000>
- Stassun, K. G., Oelkers, R. J., Pepper, J., et al. 2018, *AJ*, 156, 102
- Stumpe, M. C., Smith, J. C., Catanzarite, J. H., et al. 2014, *Publications of the Astronomical Society of the Pacific*, 126, 100. <https://doi.org/10.1086%2F674989>
- Stumpe, M. C., Smith, J. C., Cleve, J. E. V., et al. 2012, *Publications of the Astronomical Society of the Pacific*, 124, 985. <https://doi.org/10.1086%2F667698>
- Taaki, J. S., Kamalabadi, F., & Kemball, A. J. 2020, *The Astronomical Journal*, 159, 283
- Thompson, S. E., Coughlin, J. L., Hoffman, K., et al. 2018, *The Astrophysical Journal Supplement Series*, 235, 38.
<https://doi.org/10.3847/1538-4365/aab4f9>
- Twicken, J., Caldwell, D. A., Davies, M. D., et al. 2019, in *American Astronomical Society Meeting Abstracts*, Vol. 233, *American Astronomical Society Meeting Abstracts #233*, 140.03
- Twicken, J. D., Chandrasekaran, H., Jenkins, J. M., et al. 2010, in *Software and Cyberinfrastructure for Astronomy*, Vol. 7740, *International Society for Optics and Photonics*, 77401U
- Twicken, J. D., Jenkins, J. M., Seader, S. E., et al. 2016, *The Astronomical Journal*, 152, 158.
<https://doi.org/10.3847/0004-6256/152/6/158>
- Van Trees, H. L. 2001, *Detection of Signals—Estimation of Signal Parameters* (John Wiley Sons, Ltd), 239–422.
<https://onlinelibrary.wiley.com/doi/abs/10.1002/0471221082.ch4>
- Wasserman, L. 2013, *All of Statistics: A Concise Course in Statistical Inference*, Springer Texts in Statistics (Springer New York).
<https://books.google.com/books?id=qrcuBAAAQBAJ>
- Weldrake, D. T., Sackett, P. D., Bridges, T. J., & Freeman, K. C. 2005, *The Astrophysical Journal*, 620, 1043
- Wheeler, A., & Kipping, D. 2019, *Monthly Notices of the Royal Astronomical Society*, 485, 5498.
<https://doi.org/10.1093/mnras/stz775>
- Wong, I., Shporer, A., Daylan, T., et al. 2020, *The Astronomical Journal*, 160, 155.
<https://doi.org/10.3847/1538-3881/ababad>